Power System Protection and Control
ISSN:1674-3415

DEVELOPMENT OF A FLAGELLUM-INSPIRED MEMS HYDROPHONE WITH BIOMIMETIC STRUCTURES FOR ENHANCED LOW-FREQUENCY ACOUSTIC SENSING

Saeid Sakhaa, H. Fazeli[1], Jafar Eskandari Jam[2]*

[1]Mechanical Engineering Department, Malek Ashtar University of Technology, Tehran, Iran
[2]Composite Materials Department, Malek Ashtar University of Technology, Tehran, Iran
* eskandari@mut.ac.ir

Received: 22/11/2025 **Revised**: 26/12/2025 **Accepted**: 28/01/2026

***ABSTRACT*:**

This study presents a novel MEMS vector hydrophone utilizing a flagellum-inspired structure for enhanced underwater acoustic sensitivity. The hydrophone employs piezoresistive technology with a biomimetic design that integrates cilia-like structures, a four-beam linkage, and Wheatstone bridge connections. Simulations conducted in COMSOL Multiphysics revealed significant improvements in sensitivity and frequency response due to optimized structural parameters and materials. A parametric sweep demonstrated that cilia height and pole thickness were critical factors affecting natural frequency and stress distribution, with cilia heights of 2000 µm and pole thicknesses of 10 µm achieving optimal performance. The hydrophone demonstrated a linear frequency response in the 20–500 Hz range, with an eigenfrequency peak at 652 Hz, confirming operational stability outside resonance. Stress analysis showed a maximum value of 60 kPa on poles under 1 Pa acoustic pressure, with higher stress concentration achieved by increasing cilia width and height. The electrical output from the Wheatstone bridge circuit yielded a sensitivity of -211 dB (re: 1 V/µPa), substantially improving over conventional designs. The proposed hydrophone achieves a broader bandwidth and higher sensitivity than existing models, making it suitable for applications requiring precise directional and low-frequency acoustic sensing. This work highlights the effectiveness of biomimetic principles and MEMS technology in developing compact, cost-efficient hydrophones, advancing capabilities in underwater acoustic research and marine biology.

***Keywords**: MEMS; Vector Hydrophone; Flagellum-Based Structure; Sensitivity; cilium;*

INTRODUCTION

Scientists have long been fascinated by the underwater world and the sounds it holds. Today, marine biologists use underwater recordings to analyze the behaviour of marine mammals and other creatures. However, a key challenge remains: pinpointing the location and direction of multiple underwater sound sources simultaneously. This ability would be invaluable in understanding whale migration patterns and even the mystery behind mass strandings.

To achieve this, a global community of researchers focuses on developing compact, cost-effective, and scalable sensor arrays that can be integrated into a single chip. This pursuit has its roots in research from 1956, which measured underwater particle velocity and sparked efforts to determine both the magnitude and direction of sound waves (1) . The advent of microelectromechanical systems (MEMS) technology led Boston University to create a MEMS hydrophone in 1999. This device can detect sound field variations by sensing the reflections of a laser beam (2).

Various countries, particularly China, have explored different vector hydrophone mechanisms, such as moving coil (3), velocity, piezoelectric (vibration) (4), piezoresistive (5), and fiber optic hydrophones (6). This has resulted in various scalar and vector acoustic sensors with varying functionalities.

Piezoelectric hydrophones have demonstrated optimal performance and have been widely used for decades. Their advantages include high production capacity, low cost, excellent piezoelectric coefficients, and the availability of various piezoelectric materials (7). However, they also possess drawbacks such as large size, susceptibility to electromagnetic interference, potential corrosion in harsh environments, the need for protective coatings (which

DOI: 10.46121/pspc.54.1.8

reduce efficiency at high hydrostatic pressures), circuit disruptions (especially underwater), fragility, and potential breakage under high pressure, limited cable length due to high electrical impedance, narrow frequency bandwidth, sensitivity dependence on resonance frequency, poor multiplexing capabilities, and unsuitability for extreme conditions like high temperatures, high voltages, strong electromagnetic fields, and potential explosions (7).

Beyond scalar information like pressure, a wealth of vector information exists at any given point in a sound field, including pressure gradients, acceleration, particle velocity, and acoustic energy flux. With their drive toward miniaturization and integration, MEMS technology and integrated circuits (ICs) have played a crucial role in unlocking significant advantages for vector hydrophones. These advancements allow a single hydrophone to function as a complete vector sensor, providing a comprehensive understanding of the sound field. This integration has reduced the size and cost of hydrophones and improved their performance and versatility, making them a key tool in underwater acoustic research.

MEMS vector hydrophones are primarily categorised into three types based on their transduction mechanism: capacitive, piezoresistive, and piezoelectric (8). While capacitive vector hydrophones generally offer high sensitivity, the narrow gap between their capacitor plates, which are in contact with a viscous fluid, introduces viscous damping that ultimately limits their performance. Piezoresistive MEMS hydrophones, the focus of this paper, boast a simple structure and ease of fabrication making them suitable for detecting low-frequency signals. However, they suffer from low sensitivity due to the inefficient energy transfer of piezoresistive materials and are prone to thermal noise (9).

The study of MEMS hydrophones has steadily progressed and matured, marking significant milestones. In 1994, Draper Laboratory reported designing and fabricating fluid-filled variable capacitor hydrophones based on MEMS technology, implemented on a 3-millimeter silicon chip (10). This was followed by creating an 8 cubic centimeter acoustic velocity hydrophone using MEMS technology in 1996, driven by the US Navy's need for smaller hydrophones. This marked a significant step, likely the first reported instance of a MEMS vector hydrophone serving as a directional underwater acoustic sensor (11).

In 2000, a MEMS hydrophone on a silicon wafer was developed using n-type metal-oxide-semiconductor (NMOS) technology and PVDF piezoelectric material (12). A 2002 report in *Bioinspiration & Biomimetics* opened new avenues in hydrophone design and fabrication by drawing inspiration from the lateral line organ in fish. That year, Fan et al. introduced an artificial lateral line flow sensor (13).

After years of development, Zhang et al. created a biomimetic MEMS-based cilium vector hydrophone for low-frequency applications in 2004 (14). This hydrophone achieved a sensitivity of -189 dB. In 2006, Li et al. fabricated a piezoresistive MEMS hydrophone based on silicon-on-insulator (SOI) technology, exhibiting a high resonance frequency of several kilohertz (15). Uma et al. then proposed a design in 2007 for integrating a PDVF thin film with a metal-oxide-semiconductor field-effect transistor (MOSFET) preamplifier to advance MEMS hydrophone development (16) further.

Chen et al. had designed a cilium MEMS vector hydrophone on a four-beam microstructure, drawing on bionic theory and acoustic vibration principles in 2008 (17). Its packaged rubber cap was filled with silicone oil to enable simultaneous vibration of the fiber and particles. This design offered compactness, high consistency, and good directionality. Advancements in MEMS hydrophone technology continued into the 2010s. A micromachined hydrophone based on the piezoelectric effect with hydrostatically balanced air backing was developed (18). Drawing inspiration from the lateral line of fish, Guan et al. designed and fabricated a T-shaped vector hydrophone using MEMS technology in 2012 (19). A multilayer hydrophone utilizing 3-1 piezocomposite was fabricated in 2014 (20). In 2015, Linxian et al. investigated a dual T-shaped bionic MEMS hydrophone to achieve smaller size and higher sensitivity (21). Addressing the need for increased bandwidth, Mengran et al. developed a four-unit microstructure array on a single chip in 2015 (22). Furthermore, a transparent acoustic cap capable of enhancing sensitivity was designed and fabricated in 2015 (23). Perhaps one of the most notable MEMS-based designs in recent years is the bio-inspired cilium-type MEMS vector hydrophone, as depicted in Figure 1. This design showcases how nature has inspired the development of bionic MEMS vector hydrophones. These hydrophones consist of a four-beam microstructure with a rigid cylinder fixed at its center. Each beam is equipped with one or more piezoresistors (24).

DOI: 10.46121/pspc.54.1.8

Power System Protection and Control
ISSN:1674-3415

This "CFVH" design offers several advantages, including hydrophone miniaturization, rigid mounting, good low-frequency performance, and vector capabilities. However, its limitations include low sensitivity, narrow bandwidth, off-center cilia, two-dimensionality, left-right ambiguity, and other challenges.

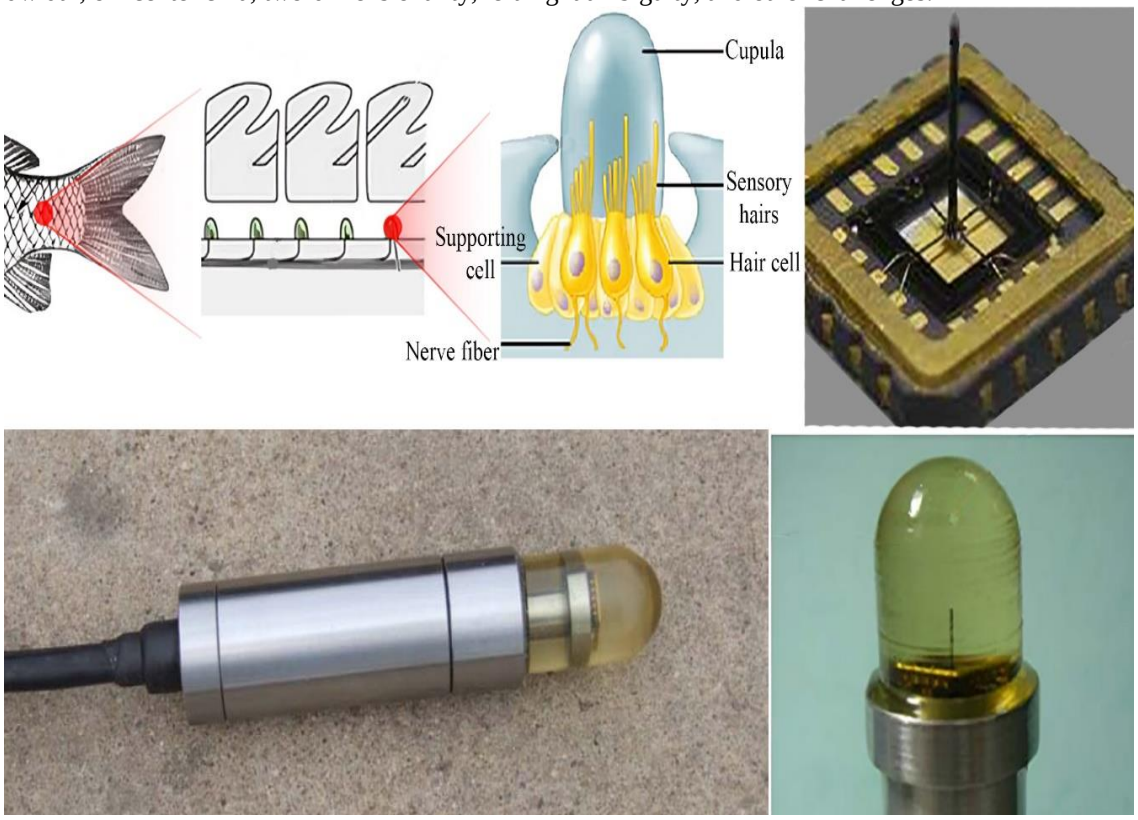

Figure 1. Different components of a four-beam cilium-type bionic MEMS hydrophone inspired by a fish's lateral line (24; 25; 26).

Figure 2.

In 2015, Zhang and colleagues introduced an innovative structure that boosted the sensitivity of conventional designs by 1.5 times, though this came at the cost of limiting the bandwidth to 500 Hz (27). That same year, Han et al. replaced the mechanical receivers in a vector hydrophone with piezoelectric transducers using PMN-PZT ceramics (28). Also, in 2015, Liu et al. proposed a "lollipop" (LVH) MEMS vector hydrophone (Figure 2a) by attaching a low-density sphere to a CFVH, effectively expanding the sensing area (29). This design improved sensitivity by 10 dB compared to the conventional CVH.

Smitha et al. employed COMSOL software in 2015 to investigate the piezoresistive effect of p-type silicon across a range of pressure variations (30). Seeking to enhance sensitivity and bandwidth, Mengran et al. proposed a hydrophone in 2016 featuring a 2x2 array of cilia configured on a single chip (Figure 2b). They explored the effects of varying cilia lengths (22). This microstructure achieved a high sensitivity of -189 dB (without a preamplifier) and a broader bandwidth of 20 to 5000 Hz.

Kumar et al. refined the design in 2016 by introducing a modified arrangement of twisted beams (Figure 2c), which increased sensitivity by effectively lengthening the beams (31).

DOI: 10.46121/pspc.54.1.8

Power System Protection and Control
ISSN:1674-3415

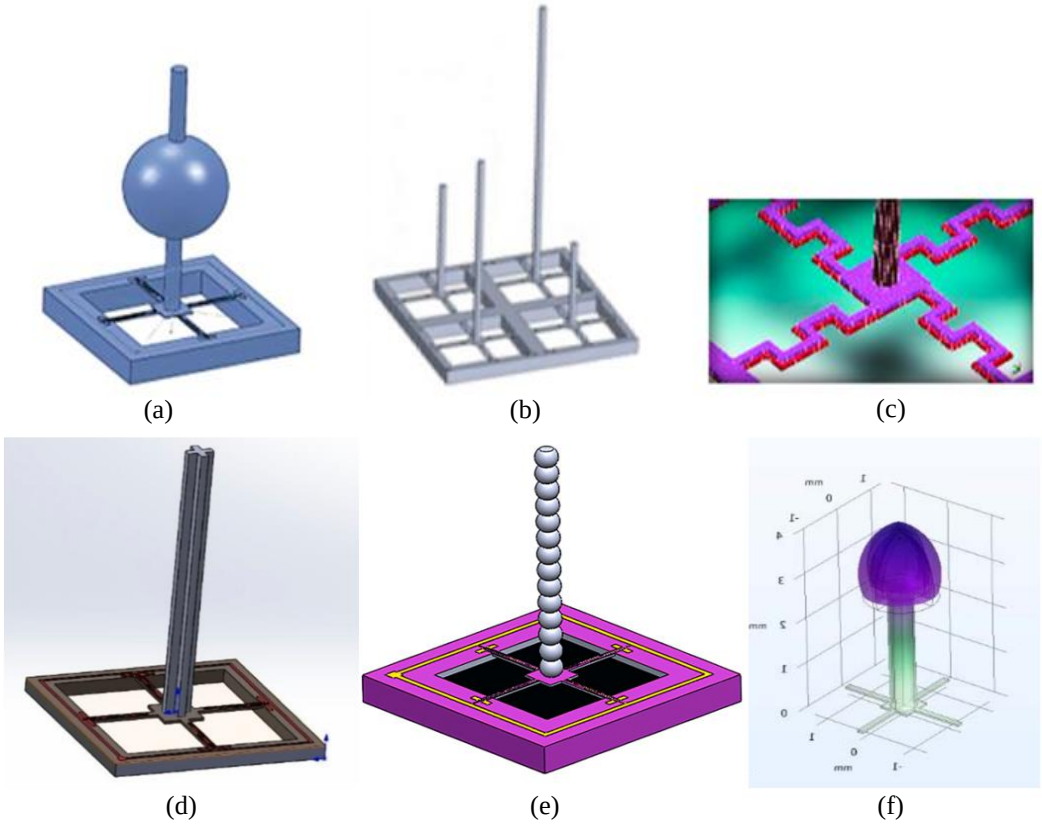

Figure 3. a) Lollipop vector hydrophone (LVH) structure (29) b) Configuration of a 2×2 array of cilia on a chip (22) c) Modified twisted beams (31). d) Hydrophone presented by Chen with a plus-shaped (+) cilium (32). e) Hydrophone presented by Elwy with a beaded cilium (33). f) Hydrophone presented by Geng with a hollow mushroom-shaped cilium (34).

In 2016, Xu et al. sought to increase the sensing area by integrating a low-density cup with a cilium structure, achieving a sensitivity of -188.5 dB and a bandwidth of 20 Hz to 1 kHz, which proved more stable than the LVH design (35). However, fabricating the LVH cilia and cup structures was complex, with low yields and increased load on the crossbeams. To address these issues, Xu et al. developed a two-component cylindrical cilium (TCVH) structure in 2018 using a simplified fabrication process (36). This optimized structure achieved a sensitivity of -188.1 dB and bandwidth ranging from 20 Hz to 1 kHz.

Singh et al. refined the CFVH design 2019 by optimizing various structural parameters (37). That same year, Zhang et al. designed a MEMS vector hydrophone with a clustered cilium (CCVH) structure, achieving an optimal size. This configuration improved sensitivity to -183.3 dB without adding appendages to the cilia or compromising bandwidth (38).

Chen et al. introduced a MEMS vector hydrophone with a plus-shaped (+) cilium in 2021, operating within a frequency range of 20 to 1000 Hz. This design increased sensitivity by 13.1 dB, reaching -184.2 dB (Figure 3a) (32). Elwy et al. also presented a MEMS vector hydrophone with a beaded cilium structure (Figure 2e), which further enhanced sensitivity by 13.5 dB, 13.7 dB, and 15 dB compared to the CVH, reaching -183.3 dB (33). Most recently, in 2023, Geng et al. proposed a hydrophone with a hollow mushroom-shaped cilium (Figure 2f), achieving a sensitivity of -180.9 dB while maintaining a frequency range of 20 to 1000 Hz (34).

This paper introduces and thoroughly analyses a novel MEMS vector hydrophone featuring a flagellum-based biomimetic structure to address the challenges of sensitivity and frequency response in underwater acoustic sensing. The design leverages principles inspired by natural sensory systems to achieve enhanced stress transfer

DOI: 10.46121/pspc.54.1.8

Power System Protection and Control
ISSN:1674-3415

efficiency and directional acoustic detection. Comprehensive multiphysics simulations, including acoustic, structural, and piezoresistive analyses, were performed using COMSOL Multiphysics to evaluate the hydrophone's performance under various geometric and material configurations. The study systematically investigates the effects of design parameters, such as cilia height and beam thickness, on natural frequency, stress distribution, and sensitivity. The proposed hydrophone achieves a sensitivity of -211 dB within a 20–500 Hz frequency range, making it highly effective for low-frequency applications. Integrating piezoresistive elements with a Wheatstone bridge circuit also provides precise electrical signal outputs corresponding to acoustic pressures. This paper demonstrates the potential of biomimetic design principles to overcome the limitations of conventional hydrophones, paving the way for scalable, high-performance MEMS acoustic sensors suitable for diverse underwater environments.

THEORY AND IMPLEMENTATIONS

Problem Definition

To obtain an accurate yet simplified mechanical model, the following six assumptions have been made:

1. **Material properties:** The mechanical system is composed of a continuous, homogeneous, isotropic material that undergoes small deformations.
2. **Rigid central block:** The central block is assumed to be perfectly rigid, exhibiting no deformation.
3. **Negligible mass:** The mass of the transverse beam and the central block is considered negligible compared to other components.
4. **No lateral bending:** The lateral beam is assumed to only experience tension and compression, with no bending effects.
5. **Cilia simplification:** The cilium is simplified as a cantilever beam and analyzed using the Euler-Bernoulli beam theory.
6. **Rigid connection:** The connection between the cilium and the central block is considered perfectly rigid without any looseness or flexibility.

Simulations

The simulations were conducted using COMSOL Multiphysics 6.2 software, incorporating three modules: acoustic pressure, mechanics, and electrical. A frequency domain study was employed to study the hydrophone's behaviour over a frequency range. An Eigenfrequency study analyzed the structure's natural frequencies with varying dimensions.

The following sections outline the simulation steps, explain the relevant physical concepts involved in solving the problem, and present and analyze the results of these studies.

The biomimetic microelectromechanical (MEMS) hydrophone is a sensor based on the piezoresistive effect. It comprises flexible beams, a central block, cilia, piezoresistors, and Wheatstone bridge electrical connections, as depicted in Figure 3. According to this figure, piezoresistors are implanted at both ends of each beam. Metallic interconnections form two Wheatstone bridges in the x and y directions. The sensor's electrical output for the circuit is derived from these two Wheatstone bridges.

Sound waves propagate through the water towards the hydrophone. Upon reaching the hydrophone, the cilia sense the pressure variations and transmit them as stress to the beams.

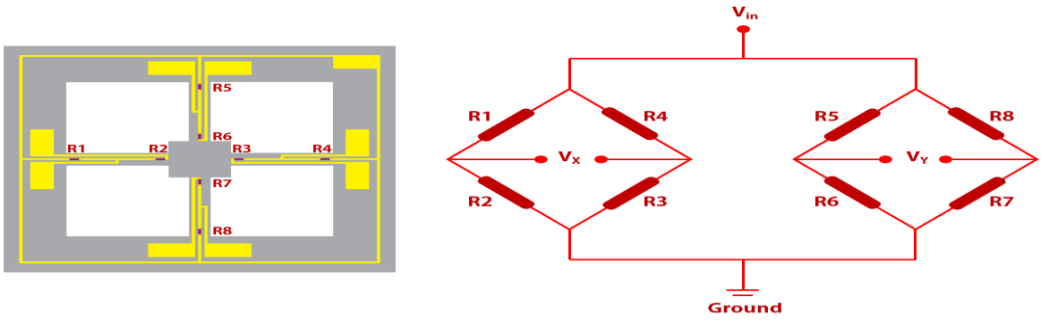

Figure 4. Piezoresistors and electrical connections of the Wheatstone bridge in two X and Y channels.

DOI: 10.46121/pspc.54.1.8

Power System Protection and Control
ISSN:1674-3415

The problem can be divided into several parts. First, we must generate an acoustic wave within a medium (water in this case). To simulate this, we require a box where the acoustic wave is generated at one end and exits or diminishes at the other, with walls that do not produce any reflections to ensure the transient acoustic wave conditions are correctly applied. Furthermore, the hydrophone structure consists of a four-bar linkage and cilia connected, experiencing deflection and stress during sensing. Next, the acoustic wave's pressure difference must be transferred to our structure. These two aspects are sufficient for simulating the hydrophone problem. However, this simulation goes a step further by implementing piezoresistive elements along with Wheatstone bridge connections on the four-bar linkage to obtain a final electrical response from the sensor.

The Acoustic-Solid Interaction module is crucial for simulating acoustic pressure fields within fluids. This is essential for predicting how sound waves propagate through different media, a fundamental aspect of hydrophone functionality. In this project, the Acoustic-Solid Interaction module simulates the acoustic environment surrounding the hydrophone, enabling the prediction of the sensor's response to incoming sound waves. This is vital for assessing the hydrophone's sensitivity. The Solid Mechanics module allows for the simulation of deformations and stress distributions within solid structures, which is necessary for evaluating structural integrity and mechanical responses under various loads. This module analyses the mechanical strength and deformation of the hydrophone structure when exposed to acoustic pressure. The Piezoresistive Effect in Shells module is designed to analyze piezoresistive effects in thin structures, which is crucial for devices like MEMS. This module is employed to model changes in the electrical properties of hydrophone components due to mechanical deformation. This modeling is essential for understanding and optimizing the hydrophone's signal transduction mechanism.

Furthermore, the simulation incorporates a cohesive interaction and integration between these modules, where the output of one serves as the input for another, reflecting the interconnected nature of the physical phenomena. For instance, the pressure variations generated in the fluid medium due to the sound wave cause the cilia to deflect, inducing stress and strain on its connected links. This deformation from the solid mechanics module, in turn, serves as the basis for analyzing piezoresistive changes in the piezoresistance module within the shells, as illustrated in Figure 4. This coordination enhances the accuracy and relevance of the simulation, providing a comprehensive understanding of the hydrophone's behavior under simulated operational conditions.

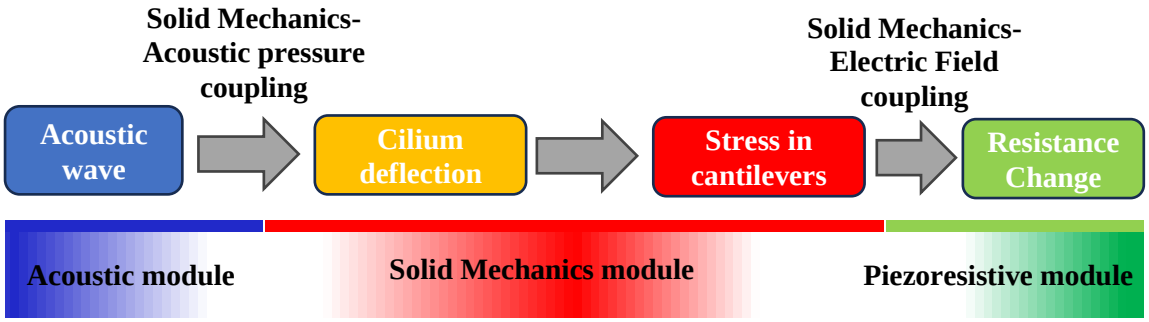

Figure 5. Schematic of the problem-solving process and the modules used.

The Solid Mechanics interface is a branch of structural mechanics based on solving the equations of motion and constitutive models for solid materials. This module calculates displacement, stress, and strain. In this simulation, Solid Mechanics is used to calculate the displacement of the cilia and the stress applied to the links. The governing differential equation for transient, time-dependent Solid Mechanics is defined as follows:

$$\rho \frac{\partial^2 \boldsymbol{u}}{\partial t^2} + d_a \frac{\partial \mathbf{u}}{\partial t} - \nabla . \tilde{\sigma} = \vec{f} \quad (1)$$

where ρ is the material density, da is the damping coefficient, σ is the stress, u is the displacement vector, and f is the body force. Its steady-state form can be rewritten as follows:

$$-\nabla . \tilde{\sigma} = \vec{f} \quad (2)$$

According to Hooke's law, the constitutive equation for a solid material follows the relationship below.

$$S - \left(S_0 + S_{ext} + S_q\right) = D(\varepsilon - \left(\varepsilon_0 - \varepsilon_{th} + \varepsilon_{hs} + \varepsilon_{pl} + \varepsilon_{cr}\right)) \quad (3)$$

In this equation, S represents stress, S_0 is pre-stress, S_{ext} denotes external stress, and S_q stands for viscous stress. ε represents elastic strain, ε_0 is pre-strain, ε_{th} denotes thermal strain, ε_{hs} represents swelling strain, ε_{pl} stands for

DOI: 10.46121/pspc.54.1.8

plastic strain, and ε_{cr} denotes creep strain. Furthermore, *D* is the elasticity matrix. However, the equilibrium and constitutive equations are insufficient to solve the problem. Acoustic equations are readily derived by linearising the equations of continuum mechanics. Considering the fundamental equations of continuum mechanics for the relatively general case of a thermoviscous fluid or a thermoelastic solid, one can obtain all that is necessary to derive the acoustic equations in complex situations. Since acoustics is defined as the small dynamical disturbances of a fluid or solid, it yields equations that must be linearized. These equations are the conservation equations, the equation of state, and the behaviour equations (39). The governing equations for lossless compressible fluid flow problems (no heat conduction and no viscosity) are the momentum equation (Euler equation) and the continuity equation, which are obtained as follows:

$$\rho\frac{\partial \boldsymbol{u}}{\partial t}+\rho(\boldsymbol{u}.\nabla)\boldsymbol{u}+\nabla p \quad or \quad \frac{\partial \mathbf{u}}{\partial t}+(\mathbf{u}.\nabla)\mathbf{u}=-\frac{1}{\rho}\nabla p$$
$$\frac{\partial \boldsymbol{\rho}}{\partial t}+u.\nabla\rho+\rho\nabla.u \quad or \quad \frac{\partial \boldsymbol{\rho}}{\partial t}+\nabla.(\rho\mathbf{u})=0 \tag{4}$$

Where ρ is the total density, *p* is the total pressure, and **u** is the velocity field. In classical acoustics, all thermodynamic processes are assumed to be reversible and adiabatic. A small-parameter expansion is performed about a quiescent fluid with density ρ0 (SI units: kg/m³) and at constant pressure *p*0 (SI units: Pa) such that:

$$\begin{matrix} p=p_0+p' \\ \rho=\rho_0+\rho' \\ u=0+u' \end{matrix} \quad with \quad \begin{matrix} p'\ll p_0 \\ \rho'\ll \rho_0 \end{matrix} \tag{5}$$

where the prime variables represent small acoustic perturbations. By substituting these into the governing equations and retaining only the linear terms in the primed variables, we can obtain:

$$\begin{matrix} \frac{\partial \boldsymbol{u}'}{\partial t}=-\frac{1}{\rho_0}\nabla p' \\ \frac{\partial \boldsymbol{\rho}'}{\partial t}+\rho_0(\nabla.\boldsymbol{u}')=0 \end{matrix} \tag{6}$$

By employing a Taylor expansion, one of the dependent variables (density) can be expressed in terms of pressure and eliminated from the equation:

$$\boldsymbol{\rho}'=\left.\frac{\partial \rho_0}{\partial p}\right|_s p'=\frac{1}{c_s^2}p' \tag{7}$$

where c_s is the speed of sound (SI unit: m/s) at constant entropy s. Finally, by rearranging the equations (divergence of the momentum equation inserted into the continuity equation) and removing the primes, the wave equation for sound waves in a lossless medium is obtained as follows (subscripts are omitted):

$$\frac{1}{\rho c^2}\frac{\partial^2 p}{\partial t^2}+\boldsymbol{\nabla}.\left(-\frac{1}{\rho}(\nabla p-\mathbf{q}_d)\right)=Q_m \tag{8}$$

The speed of sound is related to the compressibility of the fluid in which the waves are propagating. ρ_c is the bulk modulus, usually denoted by K (SI: N/m2). The equation is expanded with two optional source terms: dipole source q_d (SI: N/m3), monopole source Q_m (SI: 1/s2). For cases where the pressure changes with time, the harmonic wave can be defined as follows:

$$p(\mathbf{x},t)=p(\mathbf{x})e^{i\omega t} \tag{9}$$

Assuming the same harmonic time dependence for the source term, the wave equation for acoustic waves reduces to an inhomogeneous Helmholtz equation.

$$\boldsymbol{\nabla}.\left(-\frac{1}{\rho}(\boldsymbol{\nabla}p-\mathbf{q}_d)\right)-\frac{\omega^2 p}{\rho c^2}=\boldsymbol{Q}_m \tag{10}$$

By removing the two source terms, this equation can be used as an eigenvalue PDE to solve for eigenmodes and eigenfrequencies. To model sound waves' attenuation in lossy media, an additional first-order term in the time derivative must be introduced.

$$\frac{1}{\rho c^2}\frac{\partial^2 p}{\partial t^2}-d_a\frac{\partial p}{\partial t}+\boldsymbol{\nabla}.\left(-\frac{1}{\rho}(\nabla p-\mathbf{q}_d)\right)=\boldsymbol{Q}_m \tag{11}$$

where da is the damping coefficient, even when sound waves propagate through a lossless medium, attenuation often occurs due to interactions with the surrounding medium at the system boundaries.

The first multi-physics coupling in this simulation is between sound and structure. The acoustic-structural interface usually consists of two parts: solid and fluid. By modelling the elastic wave in the solid and the pressure

DOI: 10.46121/pspc.54.1.8

Power System Protection and Control
ISSN:1674-3415

wave in the liquid, it is possible to predict the effect of these two waves and record the behaviour of these waves at the liquid-solid interface to simulate their interface. Only full two-way coupling can realistically simulate hydrophone performance in water. The sound-structure interface includes the fluid pressure on the structure during sound propagation and the fluid's structural acceleration during the structure's movement. Its boundary condition is defined as follows.

$$\nabla\left(-\frac{1}{\rho_0}\nabla p\right)-\frac{1}{\rho_0}\left(\frac{\omega}{c}\right)^2 p=0 \qquad (12)$$

$$F_A = p_t.n$$

The simulation geometry consists of a four-pole structure and electrical subsystem on it, cilia, water box and PML layer. The four-post structure includes a base where the eyelash will be mounted in the centre. Also, according to Figure 5, eight piezoresistive elements were created two by two on the poles, which are marked with orange. All four piezoresistors form a Wheatstone bridge whose connections are marked in yellow. To reduce the complexity of the simulation and the number of mesh elements, the parts that did not affect the simulation results were removed, and the frame to which the four pillars were connected was not created. Subsequently, the connections related to Ground and constant input voltage have also been removed, and the edges marked as shown in Figure 5 will be considered terminals for connecting to ground (red colour) and input voltage (green colour).

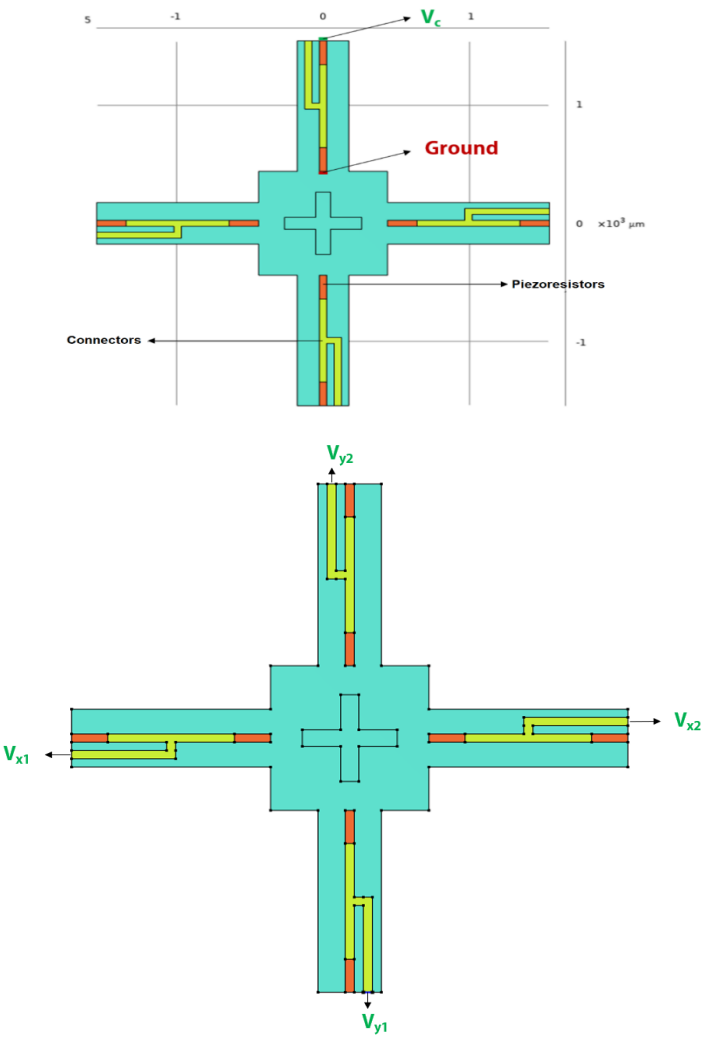

Figure 6. a) Structure of four pillars, piezoresistors and connections of Wheatstone bridge. b) Output areas of the terminal to the external electrical circuit.

DOI: 10.46121/pspc.54.1.8

Power System Protection and Control
ISSN:1674-3415

The structure of the cilia is a winged appendage, which is shorter at the base of the wings and increases at the end of the cilia. To facilitate the alignment of the cilia on the four-pillar base, a base at the end of the cilia equal to the four-pillar base is also considered, but to simplify the simulation, it was avoided in the geometry section. Finally, this structure is placed inside a box, according to Figure 6. This box will be defined as the sound wave medium, which in this study is water. According to this figure, a page is also created on the right side of the box, which will act as a PML layer.

PML layer (Perfectly Matched Layer) is an important tool for modelling acoustic and electromagnetic waves, especially in cases where wave propagation is simulated in unlimited space. The PML layer is an artificial region in the simulation model that is placed at the model's computational boundaries to minimise the waves' reflection at these boundaries. This layer is designed so that its impedance profile perfectly matches the surrounding environment, so the incoming waves pass through the boundary without significant reflection. This feature makes PML ideal for simulating processes in which waves must realistically propagate in infinite space. The use of PML in COMSOL ensures that the simulation results are closer to reality and that subsequent analyzes and reviews are based on more reliable data. The type of this Cartesian layer and the stretching type of its coordinates is Polynomial. Its scale factor is also considered as one. The simulation geometry set includes the media box and PML layer.

PARAMETRIC ANALYSIS

For the comparative study of hydrophone characteristics and behavior, the definition of geometry parameters is one of the basic steps in simulation. All geometric parameters are summarized in Table (1, 2). Geometrical parameters are divided into two categories: effective variable and dependent variable. Dependent variables are not involved in parametric studies and are defined as a function of effective variables. The effective variables include the length, width, and thickness of the pole, as well as the upper width and the height of the cilia, which are the main factors in determining the characteristics of the hydrophone. The range of changes for each of these variables in the simulations is summarised in Table 2. Due to the limitations in the methods of making eyelashes with such a high aspect ratio, its thickness is the minimum thickness that can be achieved with an acceptable quality by the SLA 3D printing method. The width of our connections and piezoresistive elements in this simulation will be considered the smallest achievable dimensions (Feature Size) in microelectromechanical manufacturing processes. Therefore, the width of the poles is considered to be seven times these dimensions because three rows of joints and four rows of the distance between the joints and the distance from the sides should be considered to fit all the joints and piezoresistive elements on the pole.

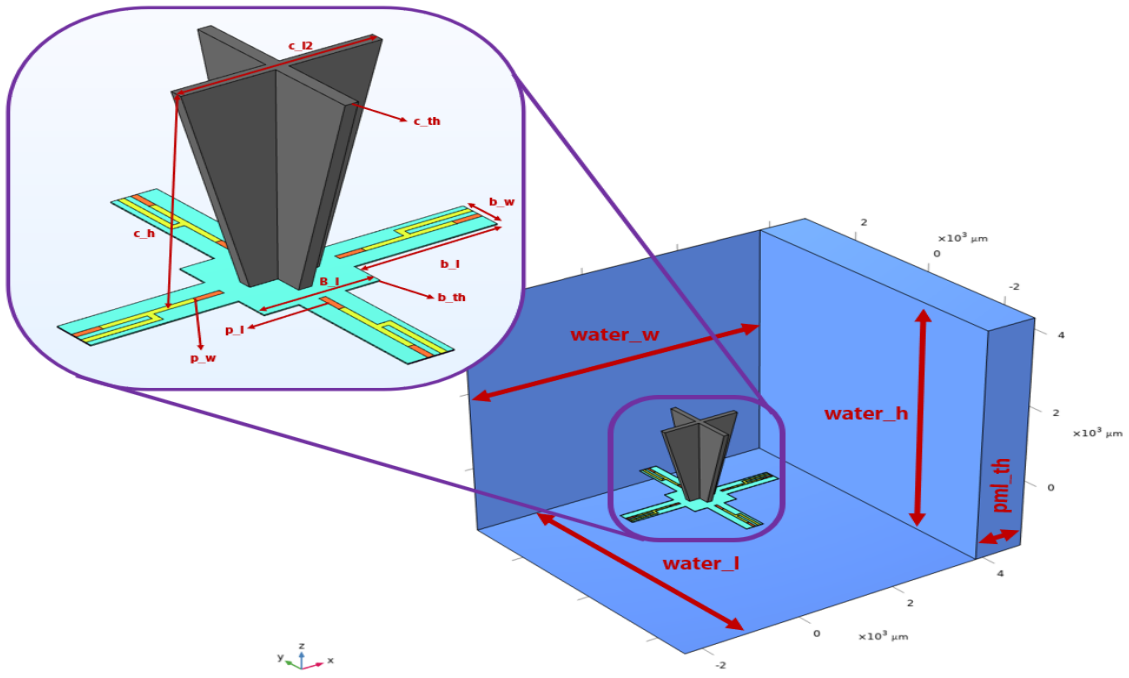

Figure 7. Schematic of geometric variables

DOI: 10.46121/pspc.54.1.8

Power System Protection and Control
ISSN:1674-3415

Table 1. Definition of geometric variables in simulation

Parameter	Value	Description
b_l	1100 µm	length of Cantilevers
b_w	350 µm	width of Cantilevers
b_th	10 µm	thickness of the Cantilevers
B_l	b_w × 2.5	length of the base of the Cantilevers
c_w	100 µm	thickness of cilia walls
c_l1	b_w × 1.5	length of cilia at base
c_l2	1500 µm	length of cilia at the top
c_h	2000 µm	cilia height
p_w	b_w/7	width of piezoresistive elements
p_l	b_l/5.5	length of piezoresistive elements
w_w	p_w	width of connections
water_l	((b_l×2)+B_l)×2	length of water media box
water_w	(((b_l×2)+B_l)×2)+pml_th	water media box width
water_h	c_h×3	height of the water media box
pml_th	1000 µm	PML layer thickness

As a result, one seventh of the width of the poles is considered as our Feature Size. According to the available facilities, the smallest available and reliable dimensions are 20 µm; Therefore, the lower limit of the range of changes in the width of the post is considered to be 140 µm, which is also reported in most references.

Table 2. Variation range of effective geometrical variables in simulation

Variable	Default value	Change limits
b_l	1100 µm	600 to 1500 µm
b_w	350 µm	140 to 420 µm
b_th	10 µm	10 to 60 µm
c_l2	1500 µm	500 to 3000 µm
c_h	2000 µm	1500 to 4000 µm

In this section, we will examine and introduce the materials used in the hydrophone simulation and the physical conditions of the environment in which the simulations were performed. Material selection and precise setting of physical and boundary conditions for each component of the structure must be done carefully to obtain a more accurate modeling of the real conditions. In the same way, in the selection of materials, care must be taken to ensure that they have the necessary properties for performing calculations. According to the explanations in the comprehensive guide of Comsol, to simulate the piezoresistive properties in the shells, n-type single crystal silicon with partial contamination should be used for the poles and p-type for the piezoresistive areas. Wheatstone bridge connections are also selected as p-type, which will be defined later in the related physical settings as areas with high conductivity, and their piezoresistive properties will be cancelled. Single-crystal silicon has non-isotropic mechanical and electrical properties. Therefore, to define its properties, a piezoresistive coupling matrix, an elasticity matrix, and an elastopiezoresistive matrix are defined and used in calculations.

For the water box and PML layer, the water material from the Comsol predefined material library is used, where the density and sound speed are defined as a function of temperature. Considering that the cilia can be made using the resin 3D printing method, which has been used in most references, conventional properties for cured resin have been considered for the cilia, whose properties are presented in Table 3.

Table 3. Properties of cured resin used in resin 3D printing

Poison Ratio	Young Modulus (Gpa)	Density (kg/m3)
0.4	1.5	2500

In the physics of solid mechanics, in the simulation, it has been applied only to the structure of four pillars and cilia, and the displacement field of Quadratic Serendipity has been used. The reference speed of sound in solids is taken from the material, and all structures are set in an elastic and non-isotropic state. One end of each quadrilateral is fixed accordingly to prevent it from moving during simulation. No other boundary conditions have

DOI: 10.46121/pspc.54.1.8

been applied in the classification of solid mechanics. It should be noted that gravitational conditions can also be used in the simulation. However, investigations showed that the number of changes without applying gravity is more tangible; therefore, its application has been avoided. In the application case, homogeneous background stress is introduced to the poles, and in the face of sound pressure, the amount of this heterogeneous stress is distributed. Discretisation in the physics of sound pressure in the frequency domain has been done with Quadratic Lagrange and domain normalisation. The reference pressure level for water is equal to 1 µPa, and the face velocity in water is called from the material properties. This physics is only defined for the water box, and the temperature and pressure are set to 293.15 K and 1 atm, respectively. The side walls are described as a soft soft boundary. The mathematical term for this boundary condition is the Neumann boundary condition, which simulates an environment without sound pressure on a boundary. This boundary condition is useful for modelling scenarios where the boundary does not reflect the sound waves inward and effectively absorbs the incoming sound waves. Since no waves are reflected at this boundary, and no sound pressure is produced, it can be used to simulate an open boundary or an infinitely large domain from which waves can escape without any reflection. It should be noted that this boundary condition should be used in cases where the distance of the source from these walls is large, and there is no need to calculate the pressure on them, as a result of which the volume of calculations is reduced.

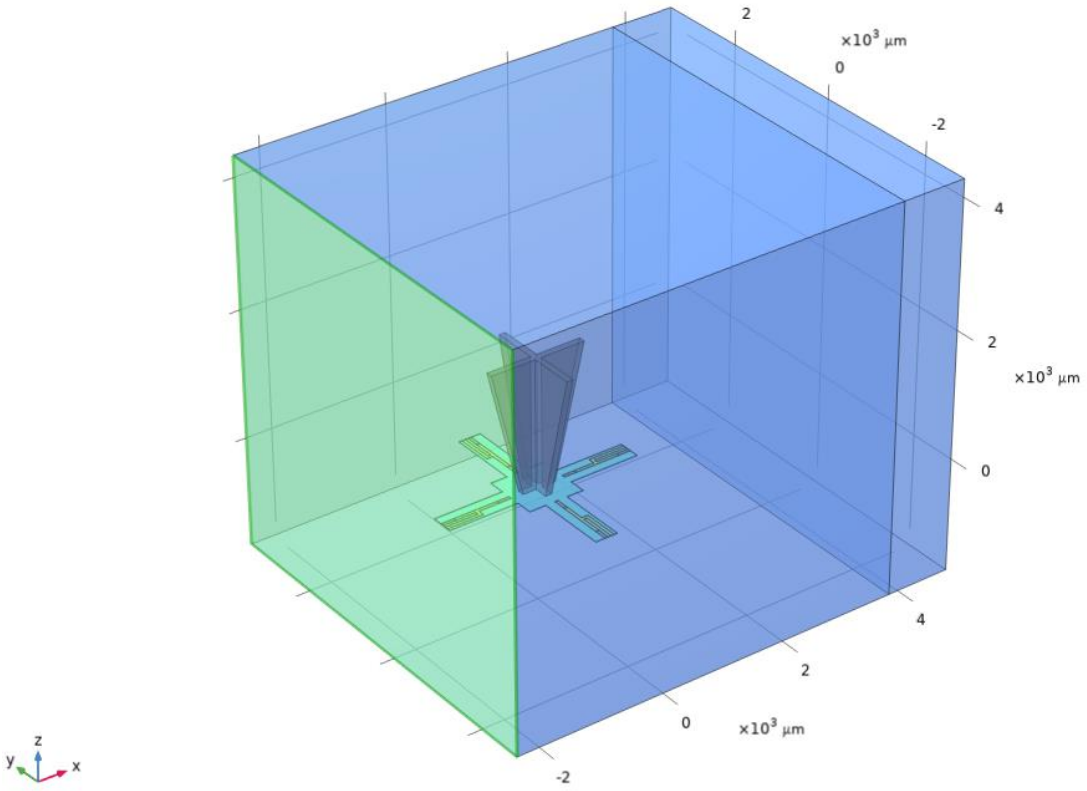

Figure 8. Sidewalls are in the water box under the sound soft boundary condition, and pressure boundary conditions are applied on the left wall of the box.

There are many ways to create sound waves. Port, Pressure, Wave Radiation, Normal Velocity, etc., as well as boundary conditions, can be used. The pressure boundary condition is used in this simulation. This boundary condition is applied to the boundaries, and pressure can be applied to one of the surfaces. According to Figure 7, the initial pressure of 10 Pa is applied to the left wall of the water box.

In addition to the physics of solid mechanics and sound pressure in the frequency domain, the physics of electric current in shells has also been added to simulate piezoresistive properties and the Wheatstone bridge. The type of shell in this physics is non-layered, and the thickness of the layer is 1 µm. According to Figure 8(a), the blue surfaces shown are considered fully conductive joints, and according to Figure 8(b), the blue surfaces shown are considered piezoresistive elements.

DOI: 10.46121/pspc.54.1.8

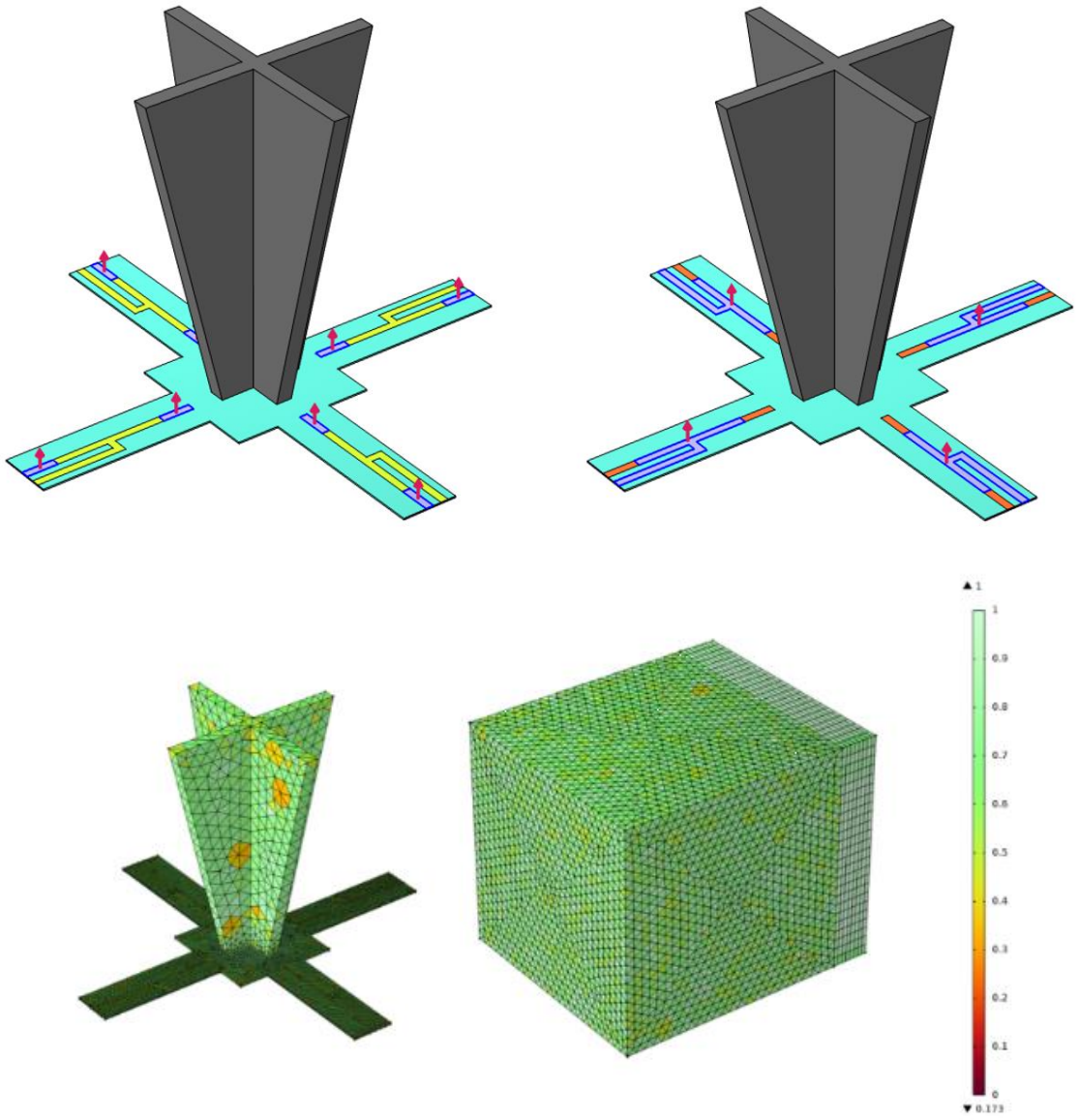

Figure 9. a) Fully conductive surfaces b) Piezoresistive surfaces. c) Structure meshing quality

The ends of the piezoresistors near the base in the four-post are connected to the ground, and the boundary condition of the ground with zero voltage is applied to it. A head of four piezoresistors at the end of the four pillars is also connected to an input electric potential equal to 5 volts, shown in Figure 8, where these boundary conditions are applied. According to Figure 8, four terminals were used for the four ends of the connections in each pole, and we chose their type as a circuit. These terminals can be connected to external circuits and receive or transmit current or voltage from the external circuit, which can be used to analyse the results of the electrical signal output after simulation.

Finally, two couples of piezoresistive physics, boundary flow and acoustic-structure boundary have been added to the simulation to transfer the results of acoustic pressure calculations to solid mechanics and from solid mechanics to electric current physics in shells.

Two approaches were followed for meshing the structure. In the first approach, as much as possible, all the meshes were manually set to Mapped, and a regular and uniform meshing was achieved. However, due to the thickness

DOI: 10.46121/pspc.54.1.8

of the poles being thin compared to their width and length, in some simulation modes, the mesh elements would inevitably have very small dimensions and lead to a huge increase in the degree of freedom, as is the case with high-powered servers. Solving the simulation takes a lot of time; Therefore, the type of meshing was automatically assigned to Comsol software according to the physics used. The sequence type is set to Physics-Controlled Mesh, and the element dimensions are set to Finer. Also, for acoustic pressure physics, the maximum dimensions of the element are controlled through Study settings. In Figure 8(c), each component's mesh quality is shown in colour. The green colour in mesh elements indicates high mesh quality, and the red indicates low mesh quality. Adding a ciliated structure to the four pillars introduces a pre-tension to the structure. It creates a deviation in the pillars, which makes it necessary to study the structure assembly's natural frequency at the simulation's beginning. Natural frequency is one of the fundamental characteristics of dynamic systems, which refers to the frequency at which a system oscillates in the absence of a driving force or damping. For any physical structure, the natural frequency is determined by the material properties (such as stiffness and mass distribution) and geometry. When a system is excited at its natural frequency, it exhibits resonant behaviour, and even small periodic forces can induce large amplitude vibrations due to the efficient storage and transfer of energy between potential and kinetic forms.

Operating a device at or near its natural frequency can lead to large amplitude oscillations that may cause mechanical failure or lead to nonlinear effects that complicate signal processing. Knowing the natural frequency allows designers to avoid these frequencies during operation or use damping strategies that reduce these effects. Additionally, in systems with multiple sensors, such as hydrophone arrays, understanding and designing for specific natural frequencies can help prevent cross-talk and destructive interference between elements. This ensures clear and reliable signal detection across the array. In conclusion, it is desirable to design the geometric design of the headphones in such a way that its working range is not within its natural frequency range. Therefore, before dealing with other studies, the effect of different geometries and parameters mentioned in the previous sections should be studied on the natural frequency.

Eigenfrequency studies have been used in COMSOL to study the natural frequency of the hydrophone. In this study, the ARPACK solver and the Around Shift search method are set in the Hertz frequency range, and the conditions of acoustic pressure physics and solid mechanics are included. The results of the studies are presented in the next section.

After that, frequency domain studies have been carried out according to the intervals announced in the definition of the problem for the effective variables. The most important factor in these studies is the maximum stress imposed on the poles and, as a result, on the piezoresistors, as a result of which the output of the electrical signal from each of the X and Y channels increases and when faced with a constant amount of acoustic pressure in In all studies, more output is received from the circuit and the sensitivity of the hydrophone increases. According to the announcement of the need, the frequency range of the hydrophone should be 20 to 500 Hz. In addition to the linearity of the responses, it should have the highest possible sensitivity in this range. The purpose of the series of natural frequency and frequency domain studies is to find a configuration of the hydrophone that, in addition to being the most sensitive, also provides a linear response in its working range, which requires that this range is outside the natural frequency values; Therefore, although some variables may result in the highest sensitivity, because the natural frequency, in that case, is in the frequency range between 20 and 500 Hz, it will not be a suitable configuration for the hydrophone.

In the first stage of the frequency domain studies, a Parametric Sweep was taken from the variables b_l, b_w, b_th, c_h and c_l2 and the maximum stress diagram on the poles, the electrical signal output from the Wheatstone bridge circuit and the sensitivity of the hydrophone were drawn by changing these variables and in In the second step, for the selected default value, a study was conducted in the frequency range of 1 to 10,000 Hz and its electrical response was recorded. The results of these simulations are reported below.

RESULTS AND DISCUSSION

Validation

In an initial comparison, according to Figure 9, it can be seen that the stress imposed on the poles as a result of the sound pressure of one pascal for different structures is in the range of several hundred kilopascals, which is close to the values obtained in the simulations of this research. However, the closest hydrophone structure to the proposed structure is the structure presented in reference (32) (Figure 13). In this structure, the poles' length, width, and thickness are 1000, 120, and 40 micrometres, respectively, and the "+"-shaped cilia have a variable

DOI: 10.46121/pspc.54.1.8

Power System Protection and Control
ISSN:1674-3415

height between 6 and 7 mm and the radius of the cilia between 0.15 and 0.25 mm. The eyelash material is made by SLA or LCD 3D printer, resin with 1450 g/cm3 density, Young's modulus of 3860 MPa, and a Poisson's ratio of 0.36. We can obtain the following results by entering these values in the model developed in this research.

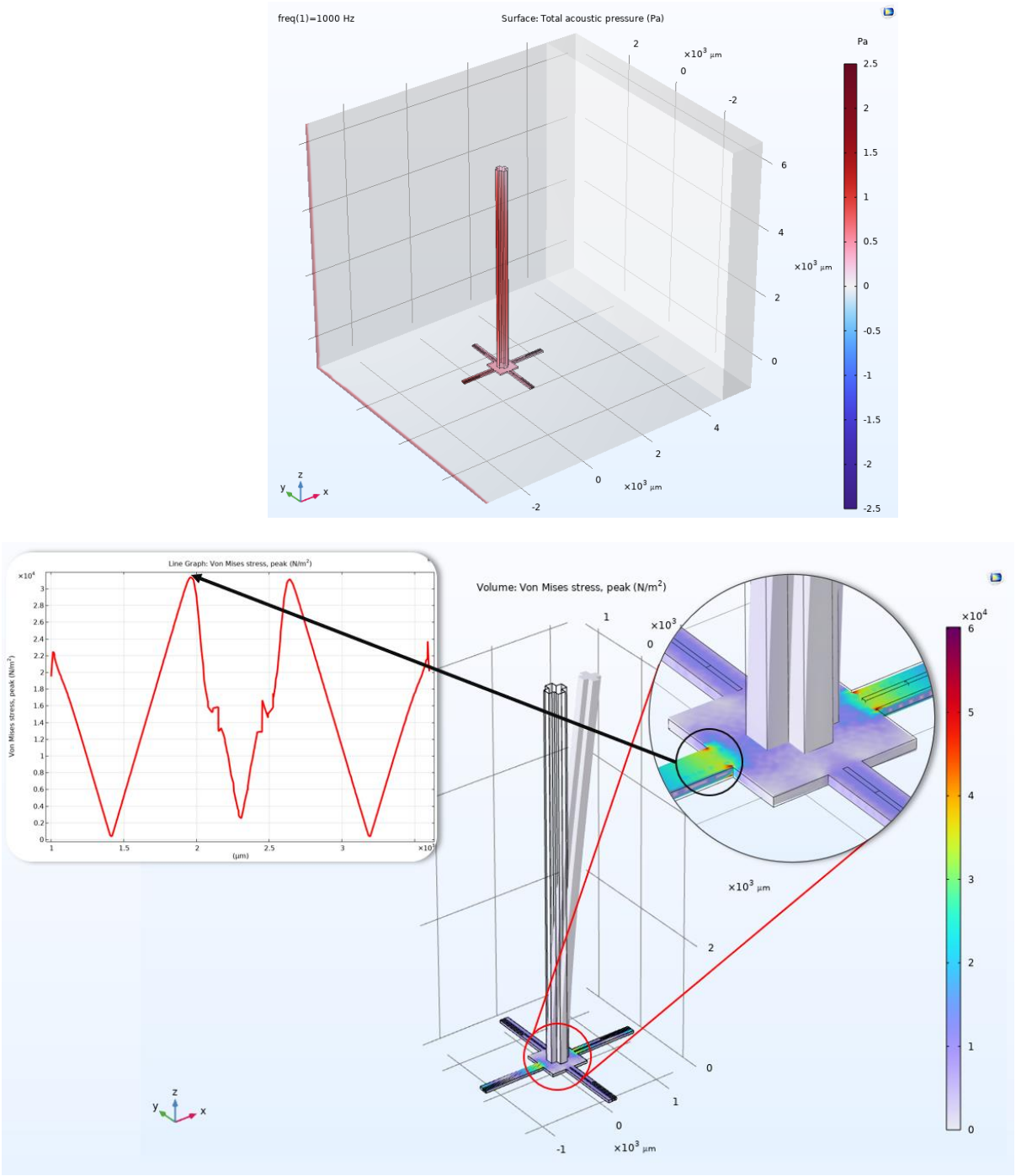

Figure 10. a) The pressure level on the hydrophone is presented in (36). b) The amount of stress on the poles (with a pressure of 1 Pa) for verification.

The geometrical values are placed in Table 1, and the simulation was carried out using three modules of acoustic pressure, solid mechanics, and piezoresistance in the shells. Each physics's limitations and boundary conditions

DOI: 10.46121/pspc.54.1.8

Power System Protection and Control
ISSN:1674-3415

are the same as those in the previous work. Still, the amount of acoustic pressure from the wall is set to 5 pascals so that the pressure on the cilia's face is 1 pascal. During each simulation stage, different amounts of acoustic pressure were applied to the wall, and by taking the double integral of the front surface of the cilia, which is exposed to the acoustic pressure, the applied pressure was calculated. Based on this, the pressure of five pascals on the wall leads to a total pressure of 1.053 Pa on the front wall of the cilia.

Table 4. Geometric values entered for reference re-simulation (32).

Parameter	Value	Description	Parameter	Value	Description
b_l	1000 µm	The length of the poles	c_h	6000 µm	eyelash height
b_w	140 µm	The width of the poles	p_w	b_w/7	The width of piezoresistive elements
b_th	40 µm	The thickness of the poles	p_l	b_l/5.5	Length of piezoresistive elements
B_l	600 µm	The length of the base of the poles	water_l	780 µm	Length of water media box
c_w	120 µm	The thickness of the cilia walls	water_w	880 µm	The width of the water media box
c_l1	300 µm	Cilia width at the base	water_h	750 µm	Height of water media box
c_l2	300 µm	The width of the eyelash at the top	pml_th	1000 µm	PML layer thickness

The sum of the absolute sound pressure divided by the selected area ((acpr.absp_t)/(c_l2*c_h)), the sum of the pressure applied to the cilia in the x direction, shows 1.0530 Pa. Based on the results of the simulation, the stress on the poles experienced values up to 60 kPa, but the amount of this stress in the middle region of the width of the poles was found to be about 31 kPa, which is acceptable close to the reference results (32). This small difference is normal due to the different models and simulation environments, and the repetition of the results of this article in the model developed in this research confirms the correctness of the results obtained in the previous stages.

Size effects

The natural frequency of the hydrophone also varies significantly with the size of the structure. In Figure 10, the effect of the parameters of the upper width of the beam and its height is studied, and in Figure 11, the effect of the parameters related to the length, width, and thickness of the four-pillar on the natural frequency is studied.

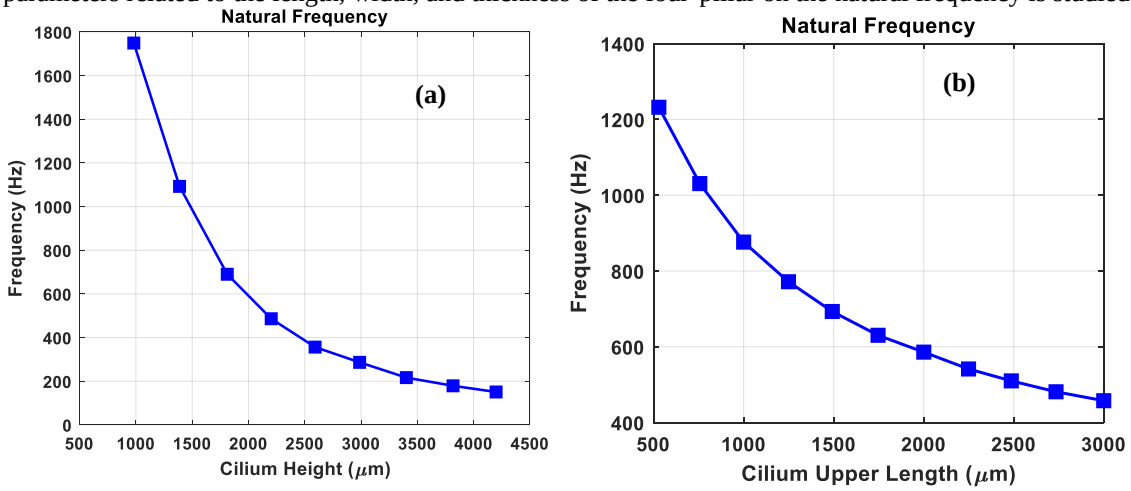

Figure 11. a) The effect of the height of the cilia on the natural frequency. b) The effect of the upper width of the cilia on the natural frequency.

DOI: 10.46121/pspc.54.1.8

Power System Protection and Control
ISSN:1674-3415

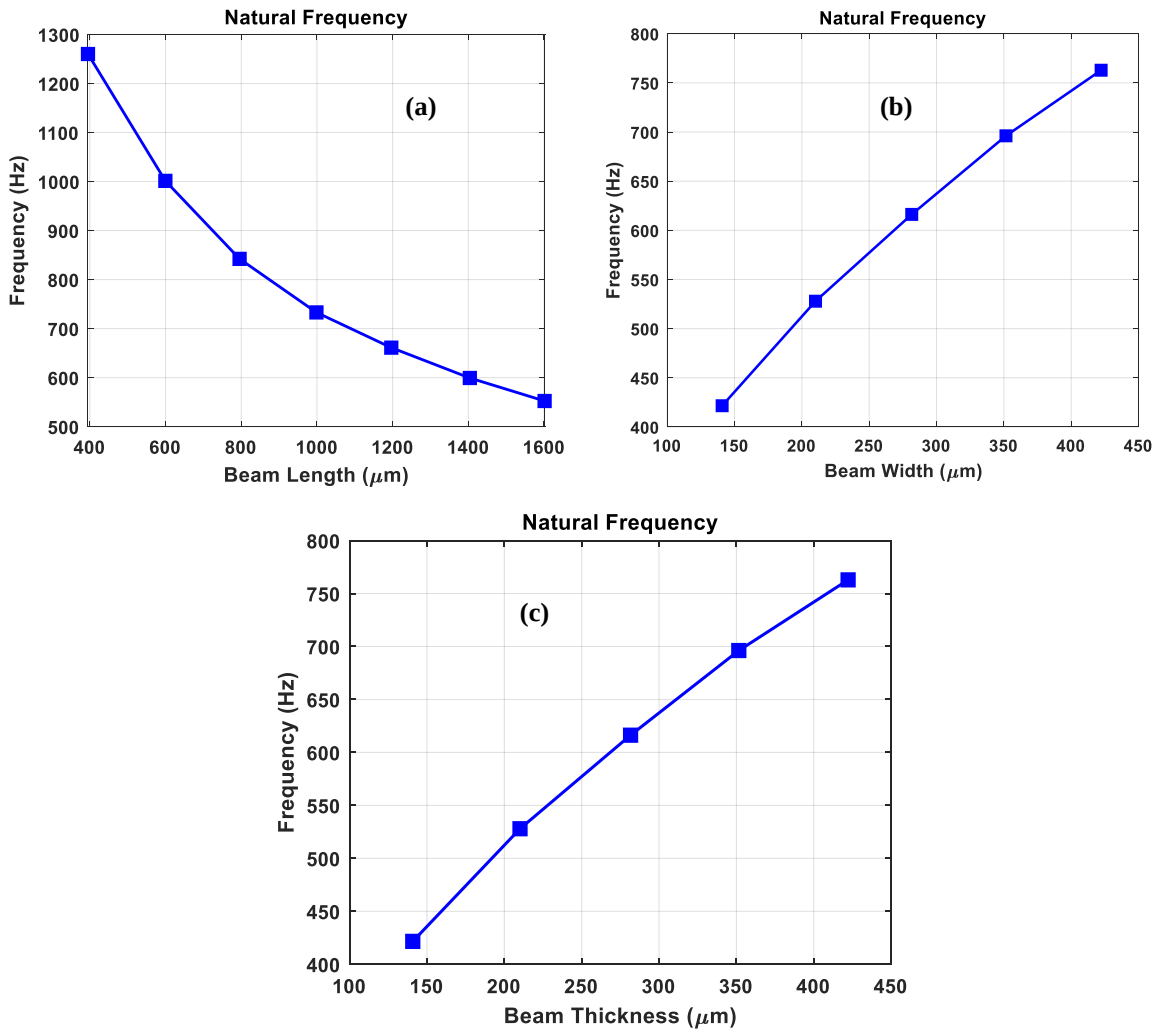

Figure 12. Effect of a) pole length, b) pole width and c) pole thickness on natural frequency.

Based on the studies, the effect of increasing the upper width and length of the cilia as well as the length of the poles has an inverse effect on the natural frequency, and with the increase of these variables, the value of the natural frequency decreases. Meanwhile, the influence of the natural frequency on the length of the pole and the upper width of the cilia is almost the same, but the height of the cilia has the greatest effect on the natural frequency. On the other hand, increasing the width of the poles and their thickness has a direct effect on the natural frequency and leads to its increase. The effect of the width of the pole on the natural frequency depends on the length of the pole and the upper width of the eyelash, but the thickness of the poles has a great role in increasing the natural frequency. Among all the studied variables, the thickness of the poles and the height of the cilia are the most important factors in determining the natural frequency of the hydrophone. On the other hand, these two factors have the greatest effect in increasing the maximum tension, which will be discussed in the next section.

Figure 12 presents mode shapes for geometric default values . The first and second resonance modes occurred at a frequency of 736 Hz. At this frequency, first in the y direction and then in the x direction, a high displacement of 2.5 micrometres occurred, transferring very high stress to the poles. After that, there was no significant deviation in the poles and the cilia, and the displacements are in the range of nanometers, which will not have a very high impact on the output signal.

DOI: 10.46121/pspc.54.1.8

Power System Protection and Control
ISSN:1674-3415

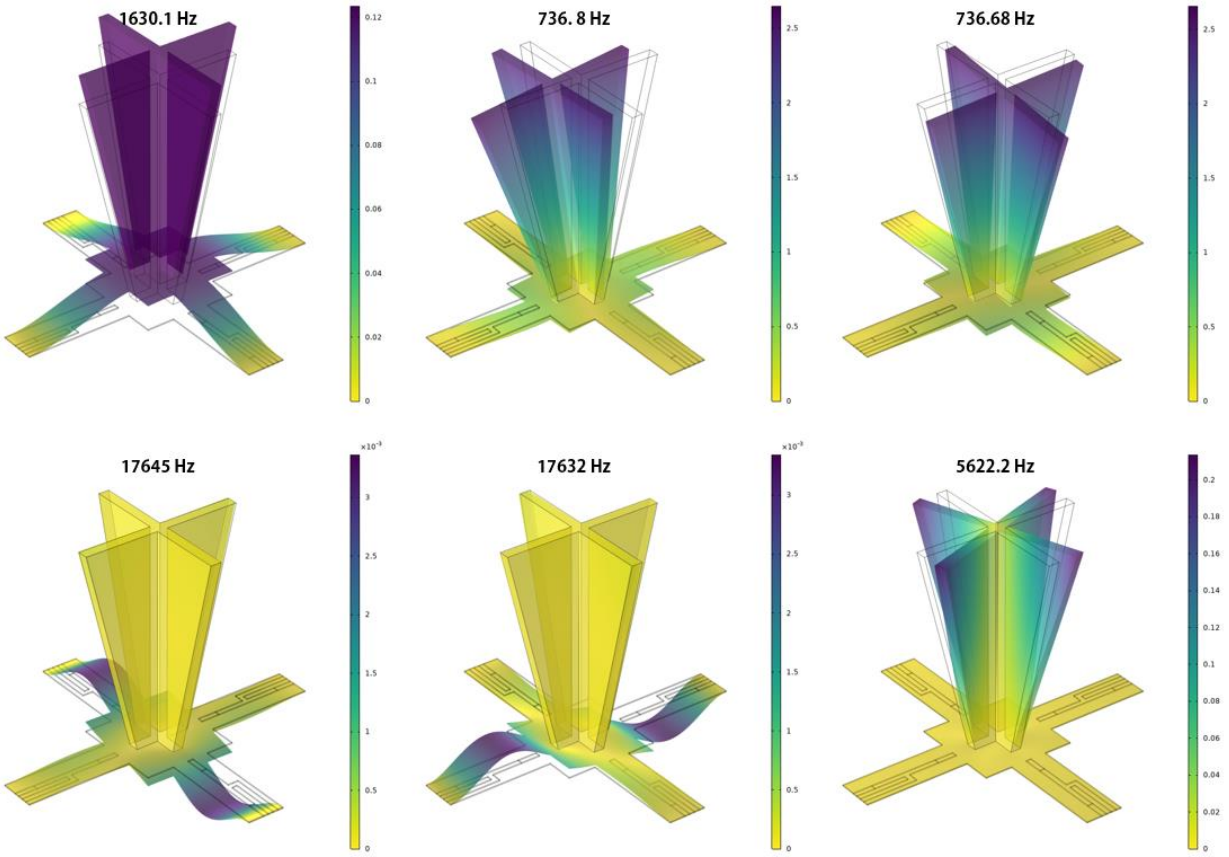

Figure 13. mode shapes for geometric default values

Another issue is the effect of different pole and cilia parameters on the maximum stress on the cilia. By increasing the amount of this tension in the poles due to constant pressure, the sensitivity of the hydrophone also increases. In Figure 13, the maximum stress diagrams are drawn on the beam to increase the length and width of different thicknesses.

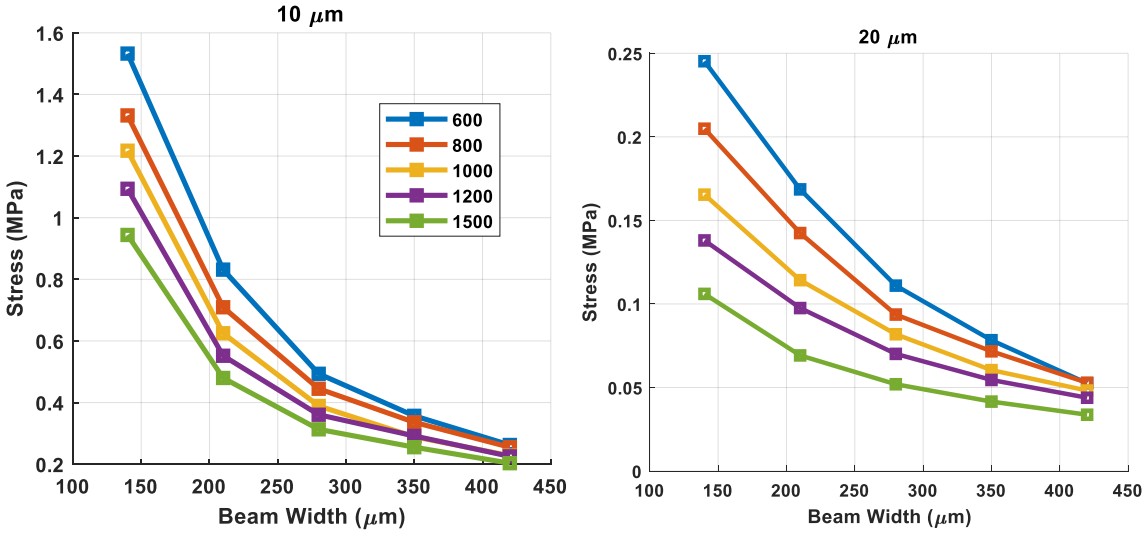

DOI: 10.46121/pspc.54.1.8

Power System Protection and Control
ISSN:1674-3415

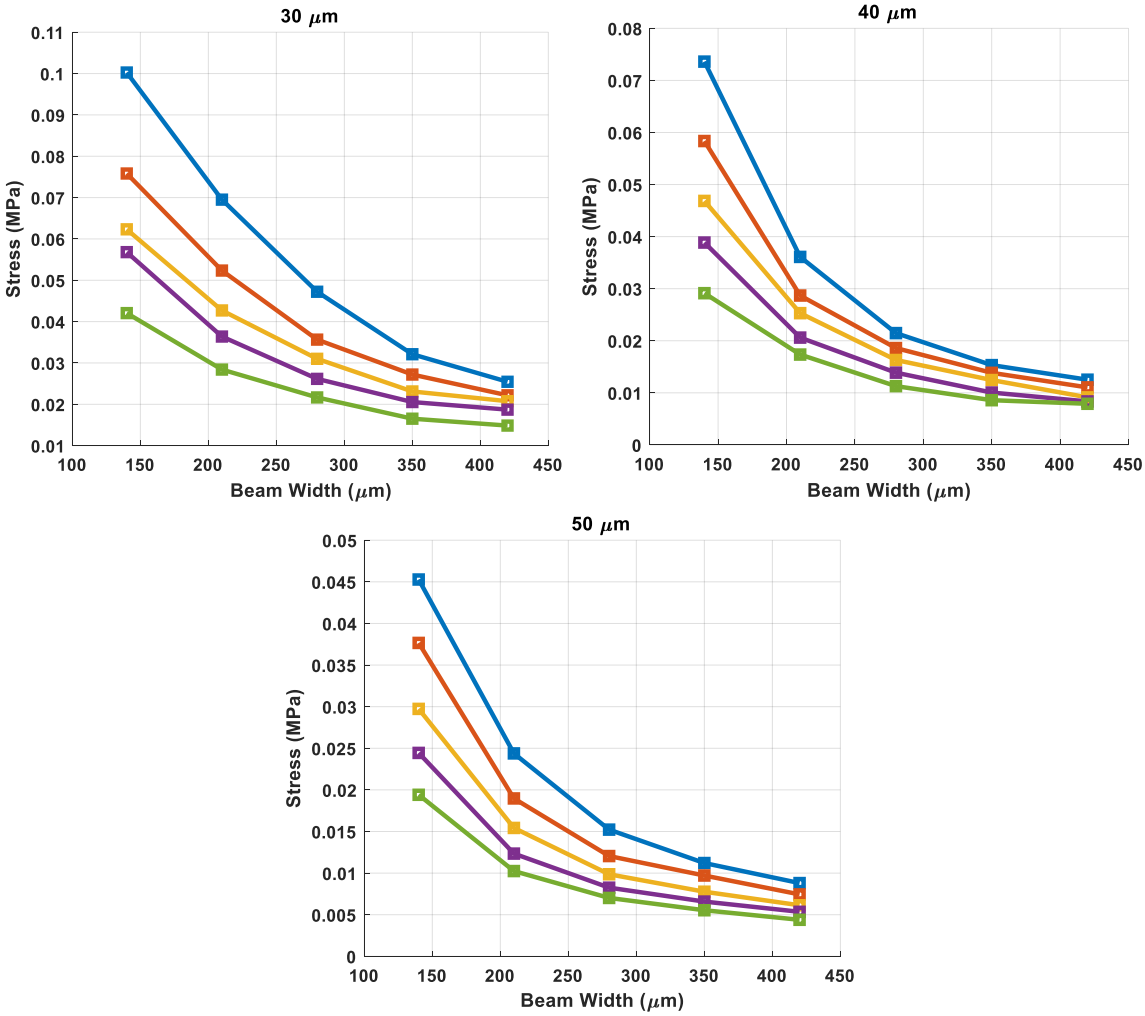

Figure 14. Diagrams of the maximum stress applied to the poles by increasing the length and width of the pole in different thicknesses.

In the first stage, it should be remembered that the level of stress on the poles decreases significantly with the increase in thickness. For example, the amount of stress on the poles at a thickness of 10 µm is in the range of MPa, and at 50 µm, it is in the range of several tens KPa. Also, increasing the width of the poles leads to a decrease in the applied stress, which has been repeated in all scenarios.

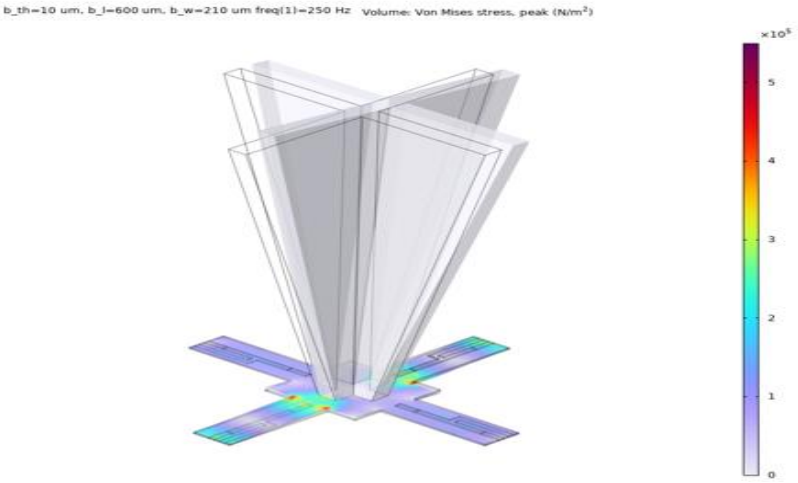

DOI: 10.46121/pspc.54.1.8

Power System Protection and Control
ISSN:1674-3415

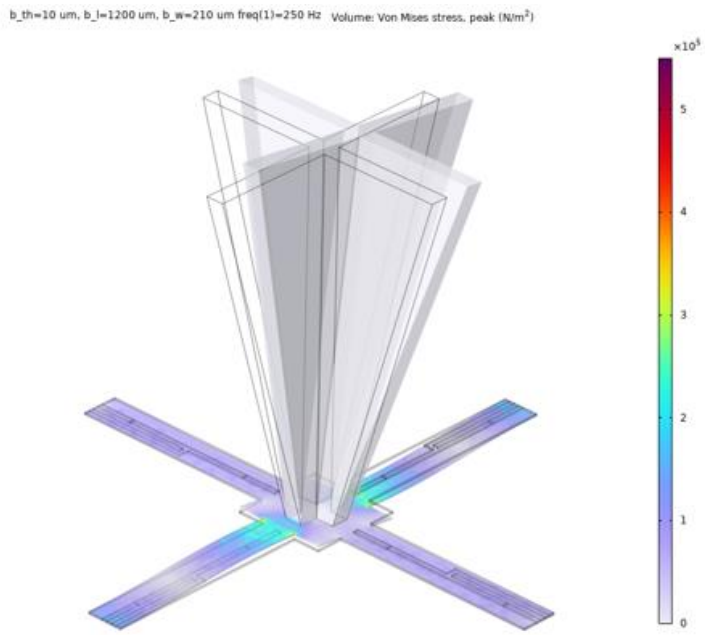

Figure 15. Comparison of the amount of stress on the poles in two different pole lengths.

However, what happens as a result of these simulations in relation to the length is the opposite, and as the length of the poles increases, the stress level decreases. The stress distribution on the poles in different lengths should be investigated to understand the reason for this issue. As shown in Figure 14, the stress level in the hydrophone with a pole length of 600 µm is higher than that of a pole length of 1200 µm. In investigating the cause of this phenomenon, it should first be considered that the amount of pressure received in the cilia, which is a constant value, leads to a specific deviation and transfers a particular stress level to the poles. By visually examining the distribution of this stress on the poles, we can conclude that this amount of stress in lower lengths has less space for distribution than in the case where the length of the poles is larger. Therefore, a higher stress level will accumulate at the beginning and end of the beam. However, in the case where the length of the poles is larger, there is more space to distribute and spread the same constant stress, and the maximum stress level naturally decreases.

On the other hand, as it is clear from Figure 15, the overall deviation of the poles increases with the increase in length, which has already been true in diaphragm pressure sensors based on MEMS. In these sensors, two areas can be defined: the middle area of the diaphragm is the area that experiences the highest amount of deviation, but the lowest amount of stress is concentrated in this area. However, the area where the diaphragm is fixed to the sides experiences the least deviation and the highest stress level, which is considered the place of planting piezoresistors because the piezoresistive property responds to the stress level. In this case, too, the shorter length of the pole leads to more concentration of stress in the connecting areas of the poles. On the other hand, by increasing the length of the poles, we have a higher stress distribution.

It should be noted that the total stress experienced increases with the increase in the length of the pole, and this issue has been investigated by integrating the stress on the surface of the pole. For example, for the case where the pole width is 210 µm, and its thickness is 10 µm, at a length of 600 µm, the total stress distributed on the surface of the poles is N 0.09974, while for a length of 1200 µm, it is N 0.1192, which shows an increase in the stress level. But this amount of stress is distributed on a larger surface and its aggregation will be less than the shorter length. As a result, increasing the length of the pole is not necessarily the right thing to do, and high sensitivities can be achieved with shorter lengths.

In Figure 15, the maximum stress applied to the poles in the case of pole width 210 µm, pole length 600 µm and pole thickness 10 µm are drawn for different widths and heights of the cilia. Based on this diagram, with the increase in the length of the cilia, we see a significant increase in the tension level in the poles. For example, for a width of 3000 µm, the maximum stress has increased 20 times by doubling the height of the cilia. Also, by

DOI: 10.46121/pspc.54.1.8

increasing the width of the beam, the applied stress increases. The reason for this is the increase in the effective level against acoustic pressure. This means that as the surface of the cilia increases, it will receive more acoustic pressure and, as a result, transfer more stress to the poles.

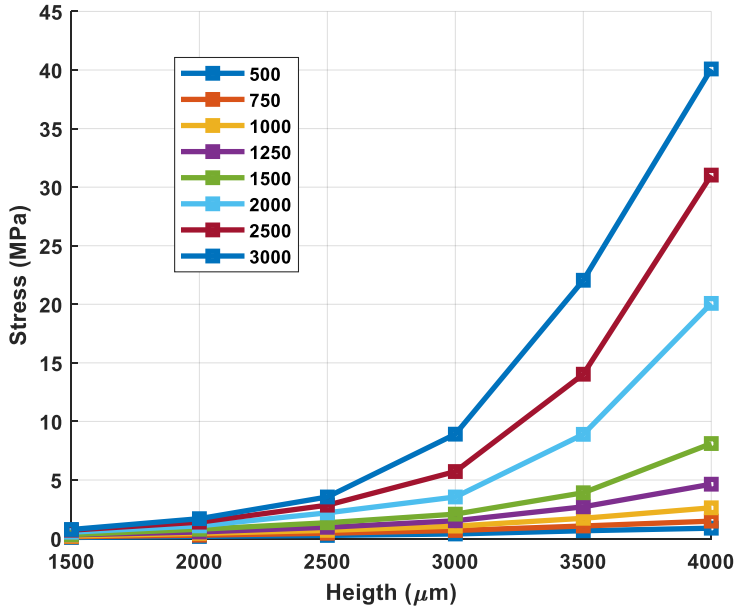

Figure 16. The maximum stress on the poles is determined by changing the upper width and the height of the lash.

The output of the Wheatstone bridge circuit in channel X is drawn in the diagram of Figure 16 in the frequency range of 1 to 10000 Hz. This is the hydrophobic electrical response diagram with a pole length of 1100 µm, pole width of 350 µm, pole thickness of 10 µm, cilia width of 1500 µm, and cilia height of 2000 µm. As it is clear in the graph, the electrical response at 652 Hz frequency presented a Sharpie peak, and before that, we see a signal drop. Naturally, the working range of the hydrophone should be in the range where a linear response to the frequency can be obtained. Therefore, according to the diagram in Figure 17, the 1 to 500 Hz frequency range can be considered for this hydrophone. Also, the 1000 Hz and above range provides a very good linear response. Still, the range of 500 to 1000 Hz is considered the forbidden range of the hydrophone frequency, and to avoid resonance, the appropriate material should be used to filter this frequency range of the acoustic wave.

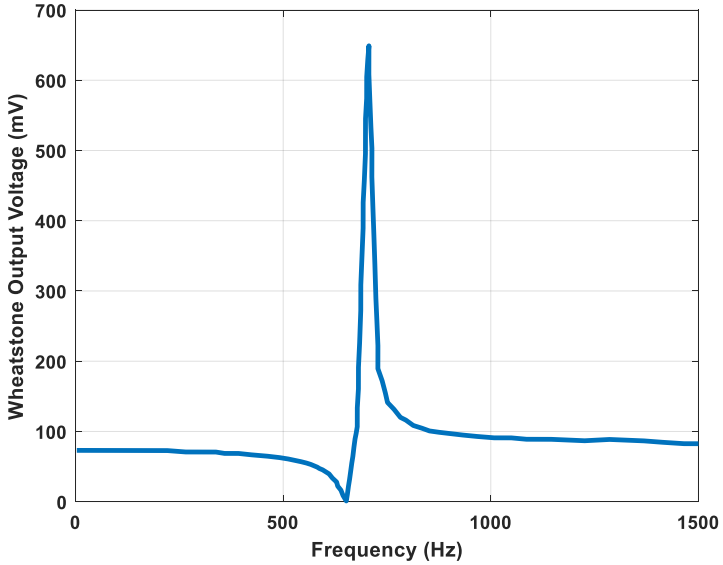

Figure 17. The electrical output diagram of the hydrophone in the frequency range of 1 to 500 Hz provides an acceptable linear value.

DOI: 10.46121/pspc.54.1.8

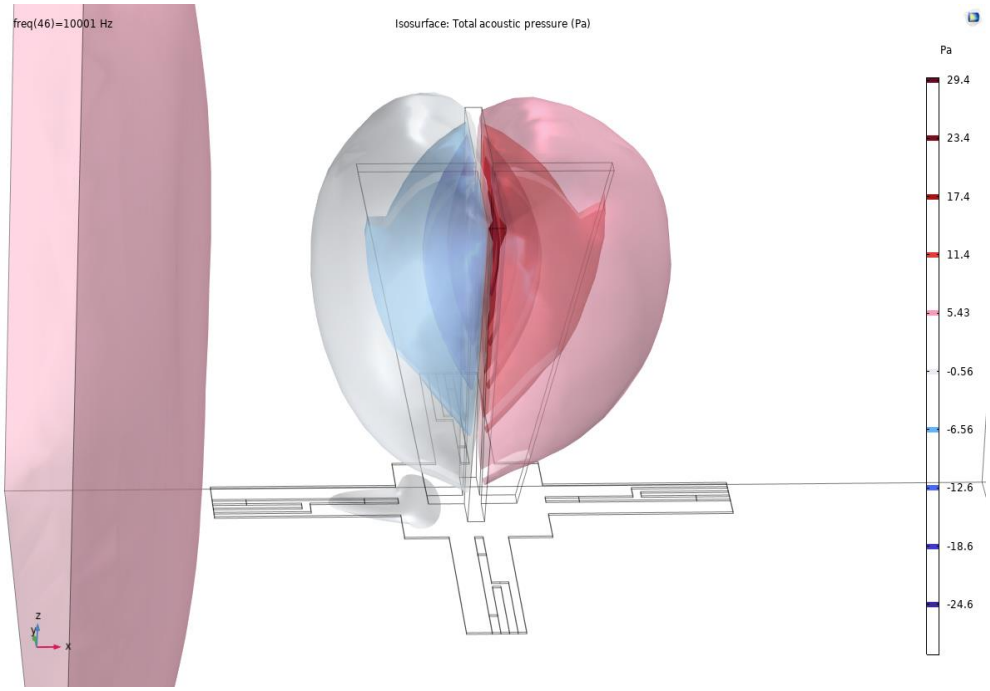

Figure 18. Acoustic constant pressure contours near the resonance frequency around the hydrophone, where it acts as a source of sound generation.

Hydrophone sensitivity converts sound pressure caused by quasi-planar sound waves into output voltage, a function of frequency. Underwater sound signals are very weak and non-contact, so the spectral density of the environmental noise pressure of the sea at 1 kHz is equivalent to 160 μPa pressure, so a very high sensitivity is needed in hydrophones [50]. It is common in underwater acoustics to specify hydrophone sensitivity in decibels (re: 1 V/Pa) rather than the simpler linear unit of mV/MPa used at higher frequencies. It can be easily shown that -240 dB (re: 1 V/μPa) is equivalent to 1 V/MPa. The hydrophone sensitivity relationship is defined as follows:

$$S = 20\log\left(\frac{\Delta U}{\Delta P \sigma^{-1}}\right) \quad (13)$$

Where ΔU changes in the hydrophone output signal as a result of the increase in sound pressure ΔP.σ-1 (V/μPa) is considered as the reference sensitivity level. For omnidirectional hydrophones, a sensitivity is defined in each dimension. Balanced omnidirectional sensitivity greatly facilitates signal processing. Another characteristic of hydrophones is the free field voltage sensitivity (FFVS). This component is defined as the RMS voltage measured from the open circuit terminals of the hydrophone in response to an input pressure of 1 μPa (40).

Having the electrical output in hand and using the sensitivity relation, we can draw the sensitivity diagram of this hydrophone. First, an integral surface should be taken from the surfaces in the X direction that receive the sound wave in the X direction, and the sum of the sound pressure values received by these surfaces should be extracted. After that, the output signal and the values of this pressure are put about the sensitivity of the hydrophone, and the graph of the sensitivity of the hydrophone in the frequency range is extracted according to Figure 17. The sensitivity of the hydrophone in the range of 1 to 500 Hz was calculated as -211 dB.

DOI: 10.46121/pspc.54.1.8

Power System Protection and Control
ISSN:1674-3415

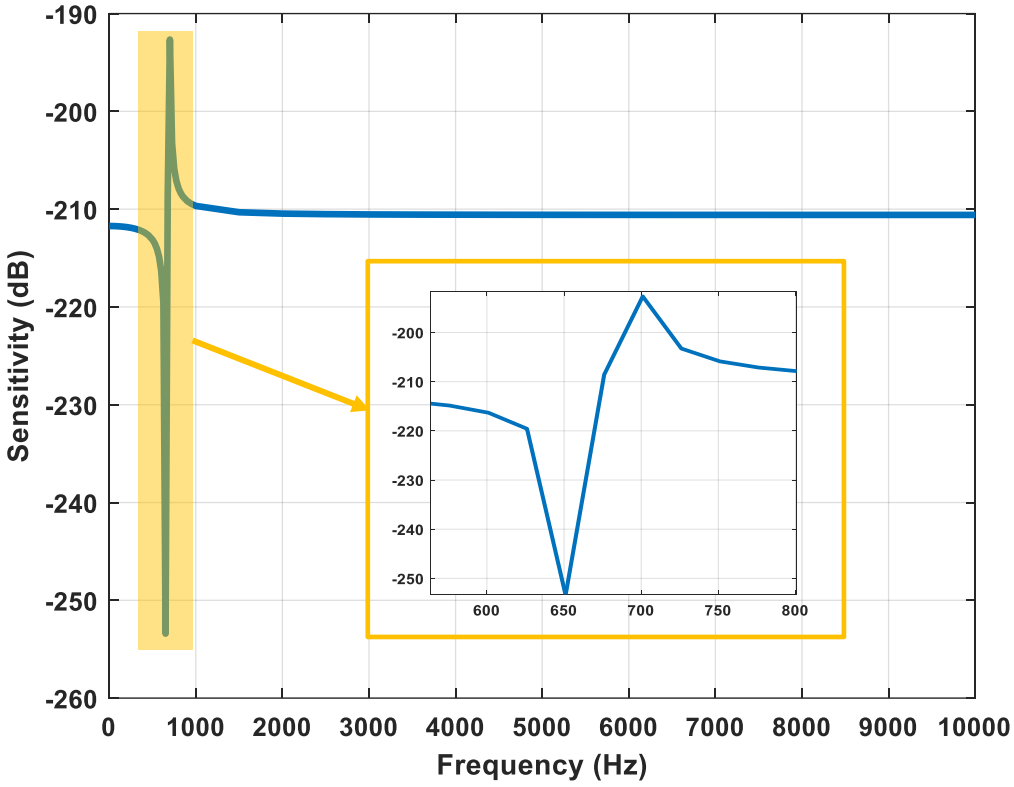

Figure 19. Hydrophone sensitivity in the frequency range of 1 to 10,000 Hz.

ENHANCED DISCUSSION: NOVEL PERSPECTIVES ON MEMS HYDROPHONE DESIGN

Advancements in Flagellum-Based Structures

The proposed MEMS vector hydrophone demonstrates a significant leap in underwater acoustic sensing by integrating a flagellum-inspired structure, achieving enhanced sensitivity and broader frequency response. The biomimetic approach, rooted in principles from natural systems, has shown promise in overcoming challenges associated with conventional piezoelectric and piezoresistive hydrophones. This unique design offers improved stress transfer efficiency while maintaining compactness and mechanical robustness. Still, it also highlights the need for further optimisation to mitigate trade-offs, such as reduced bandwidth in specific configurations.

Material Innovation and Structural Adaptability

The selection of materials, particularly single-crystal silicon for the piezoresistive elements and resin-based materials for the cilia, balances sensitivity and durability. However, leveraging emerging materials such as graphene or piezoelectric nanocomposites could significantly enhance the hydrophone's performance. These materials exhibit superior mechanical and piezoresistive properties, potentially increasing sensitivity while maintaining structural integrity. Furthermore, incorporating adaptive materials capable of responding to environmental stresses, such as temperature or salinity fluctuations, would ensure consistent performance in diverse underwater conditions.

Frequency Response and Sensitivity Optimization

The hydrophone's sensitivity of -211 dB within the 20–500 Hz range positions it well for low-frequency underwater applications. However, resonance-induced nonlinearity in the 500–1000 Hz range requires attention. Future designs could incorporate damping layers or adaptive resonance tuning mechanisms to stabilise performance across a broader frequency spectrum. This would expand the hydrophone's applicability to scenarios requiring low- and mid-frequency signal detection.

DOI: 10.46121/pspc.54.1.8

Interdisciplinary Opportunities in Biomimetic Design
The success of the flagellum-based hydrophone underscores the potential of biomimetic approaches to revolutionise underwater sensing technologies. Insights from other natural systems, such as the mechanics of jellyfish tentacles or cephalopod sensory systems, could inspire the development of more adaptable and sensitive hydrophone structures. Additionally, interdisciplinary collaboration with biology, materials science, and physics experts could further refine the integration of bioinspired features into MEMS devices.

Environmental and Economic Considerations
Miniaturised MEMS hydrophones represent a paradigm shift in underwater sensing by reducing costs and enabling scalable deployment. However, their widespread use raises concerns about environmental sustainability, particularly in ecologically sensitive marine areas. Designing hydrophones with biodegradable materials or incorporating eco-friendly fabrication processes could minimise their ecological footprint. Moreover, the compact and cost-effective design could democratise access to advanced sensing technology, broadening its application in marine research and industrial monitoring fields.

Future Directions
To further advance the field, several key areas of research should be prioritised:

1. Material Advancements: Exploring next-generation materials with superior mechanical and piezoresistive properties for hydrophone components.
2. Environmental Adaptability: Developing self-healing or self-adaptive hydrophone structures to maintain functionality in diverse underwater conditions.
3. Array Integration: Investigating integrating multiple hydrophone units into compact arrays for advanced applications such as beamforming and sound source localisation.
4. Cross-Environment Applications: Adapting the hydrophone for non-marine environments, such as air-based acoustics or aerospace structural monitoring.

CONCLUSION

The evolution of MEMS vector hydrophones has marked a significant leap forward in underwater acoustics, driven by advancements in miniaturisation, cost-effectiveness, and sensitivity. This paper presented the design, simulation, and analysis of a biomimetic MEMS vector hydrophone incorporating a flagellum-based structure to enhance sensitivity and broaden bandwidth. Drawing inspiration from nature, the design leverages the piezoresistive effect and innovative structural geometries to balance sensitivity and operational robustness in challenging underwater environments.

Our study systematically examined the effects of geometric and material parameters on the hydrophone's performance. Key insights include the critical role of pole thickness and cilia height in determining the natural frequency and maximum stress distribution, underscoring the importance of design optimisation. Integrating a Wheatstone bridge circuit further enhanced signal detection and processing capabilities, enabling a sensitivity of -211 dB in the frequency range of 20–500 Hz, which aligns with underwater acoustic requirements. Validation against existing designs confirmed the model's reliability, while parametric studies identified configurations that maximise sensitivity while avoiding resonance-induced nonlinearities.

The proposed hydrophone demonstrates significant potential for underwater navigation, marine biology, and surveillance applications. Its compact design and enhanced sensitivity and scalability address longstanding challenges in underwater acoustic sensing. Future work could explore further material optimisation, integration of noise reduction techniques, and real-world testing to refine the hydrophone for broader applications. This study advances MEMS hydrophone technology, bridging the gap between bioinspiration and practical engineering solutions in underwater acoustics.

DOI: 10.46121/pspc.54.1.8

BIBLIOGRAPHY

1. 1. Hydrophone for measuring particle velocity. Leslie, C., J. Kendall, and J. Jones,. s.l. : The Journal of the Acoustical Society of America, 1956, Vols. 28(4): p. 711-715. https://doi.org/10.1121/1.1908455.
2. 2. A novel microelectromechanical system (MEMS) design for an underwater acoustic field sensor. Bifano, T. G., Cleveland, R. O., Compton, D. A., & Pierce, A. D. USA : The Journal of the Acoustical Society of America, 1999, Vols. 105(2): p. 998-998. https://doi.org/10.1121/1.424817.
3. 3. A simple neutrally buoyant sensor for direct measurement of particle velocity and intensity in water. Gabrielson, T. B., Gardner, D. L., & Garrett, S. L. s.l. : The Journal of the Acoustical Society of America, 1995, Vols. 97(4): p. 2227-2237. https://doi.org/10.1121/1.411948.
4. 4. Shipps, J.C. and K. Deng. A miniature vector sensor for line array applications. in Oceans 2003. Celebrating the Past... Teaming Toward the Future (IEEE Cat. No. 03CH37492). 2003. IEEE.
5. 5. The µ-flown: a novel device for measuring acoustic flows. de Bree, H. E., Leussink, P., Korthorst, T., Jansen, H., Lammerink, T. S., & Elwenspoek, M. s.l. : Sensors and actuators A: Physical, 1996, Vols. Volume 54, Issues 1–3, Pages 552-557. https://doi.org/10.1016/S0924-4247(97)80013-1.
6. 6. Measurement research of the optical fiber vector hydrophone used in underwater acoustic applications in the deep ocean. Liang, Yan, Zhou Meng, Yu Chen, Jianfei Wang, and Mo Chen. s.l. : Advanced Sensor Systems and Applications, 2020, Vols. vol. 11554, pp. 260-267. https://doi.org/10.1117/12.2576134.
7. 7. Saheban, Hamid, and Zoheir Kordrostami. "Hydrophones, fundamental features, design considerations, and various structures: A review." Sensors and Actuators A: Physical 329 (2021): 112790.
8. 8. Directivity Modeling and Simulation Analysis of a Novel Structure MEMS Piezoelectric Vector Hydrophone. Deng, Wei, Qingqing Fan, Junhong Li, and Chenghao Wang. 14(8), 1495, s.l. : Micromachines , 2023. https://doi.org/10.3390/mi14081495.
9. 9. Song, Jinlong, Renxin Wang, Guojun Zhang, Zhenzhen Shang, Lansheng Zhang, and Wendong Zhang. "A monolithic integration bio-inspired three-dimensional MEMS vector hydrophone." IEEE Access 7 (2019): 102366-102376.
10. 10. Rebello, Keith J., David A. Kitchin, Robert F. Henrick, and Francisco Tejada. "Low cost MEMS hydrophones." In Optics and Photonics in Global Homeland Security III, vol. 6540, pp. 175-182. SPIE, 2007.
11. 11. Rockstad, H.K., et al. A microfabricated electron-tunneling accelerometer as a directional underwater acoustic sensor. in AIP Conference Proceedings. 1996. American Institute of Physics.
12. 12. Zhu, B., et al. Solid state MOSFET-based hydrophone. in Smart Structures and Materials 2000: Smart Electronics and MEMS. 2000. SPIE.
13. 13. Design and fabrication of artificial lateral line flow sensors. Fan, Z., Chen, J., Zou, J., Bullen, D., Liu, C., & Delcomyn, F. s.l. : Journal of micromechanics and microengineering, 2002, Vol. 12(5): p. 655. 10.1088/0960-1317/12/5/322.

DOI: 10.46121/pspc.54.1.8

14. 14. Biomimetic Cilia-based MEMS Sensors for Underwater Applications—A Review. Abdul, B., S. Abdul, and A. R. Asary. s.l. : N. Am. Acad., 2021, Vols. Res 4,11-21.
15. 15. A novel design of piezo-resistive type underwater acoustic sensor using SOI wafer. Li, Sie-Yu, Chih-Chao Hsu, Shi-Zheng Lin, and Ru-Min Chao. s.l. : Oceans Engineering, Materials Science, Physics, 2006, Vols. pp. 1-4. https://doi.org/10.1109/OCEANSAP.2006.4393840.
16. 16. Uma, G., et al., Design and Simulation of PVDF-MOSFET Based MEMS Hydrophone. Instrumentation Science and Technology, 2007. 35(3): p. 329-339.
17. 17. A novel MEMS single vector hydrophone. CHEN, Shang, Chen-yang XUE, Bin-zhen Zhang, and Bin XIE. China : Acta Armamentarii, 2008, Vols. 29(6): p. 673-677. http://www.co-journal.com/EN/Y2008/V29/I6/673.
18. 18. A micro-machined piezoelectric hydrophone with hydrostatically balanced air backing. Choi, S., H. Lee, and W. Moon,. s.l. : Sensors and Actuators A: Physical, 2010, Vols. 158(1): p. 60-71. https://doi.org/10.1016/j.sna.2009.12.019.
19. 19. Design of T-shape vector hydrophone based on MEMS. Linggang Guan, Guojun Zhang, Jiao Xu, Chenyang Xue, Wendong Zhang, Jijun Xiong. s.l. : Sensors and Actuators A: Physical, 2012, Vols. Volume 188, December 2012, Pages 35-40. https://doi.org/10.1016/j.sna.2012.01.018.
20. 20. Homogenization of PMN-PT/epoxy 1–3 piezocomposites by resonator measurements and finite element analysis. Kim, Jinwook, and Yongrae Roh. s.l. : Sensors and Actuators A Physical, 2014, Vols. 206: 97-106. DOI:10.1016/j.sna.2013.12.005.
21. 21. Linxian, L., et al., Research on double T-shape MEMS bionic vector hydrophone and its application in obstacle avoidance sonar. Sensor Review, 2015.
22. 22. Mengran, L., et al., Design of the monolithic integrated array MEMS hydrophone. IEEE Sensors Journal, 2015. 16(4): p. 989-995.
23. 23. Liu, M., et al., Design of MEMS bionic vector hydrophone based on NBR sound-transparent cap. Sensor Review, 2015.
24. 24. Zhang, W.D., et al., Research of DOA estimation based on single MEMS vector hydrophone. Sensors, 2009. 9(9): p. 6823-6834.
25. 25. Design and Experiment Research on MEMS Vector Hydrophone Vibration Damping Structure. Guo, Nan, Zhang, Guo Jun and Zhang, Wen Dong. 931-941, s.l. : Key Engineering Materials, 2015, Vols. Volumes 645-646. https://doi.org/10.4028/www.scientific.net/KEM.645-646.931.
26. 26. Naik, M.R., U. Kempaiah, and U. Kushal, Analysis of MEMS Piezoelectric Hydrophone at High Sensitivity for underwater application. Materials Today: Proceedings, 2017. 4(10): p. 10803-10809.
27. 27. Zhang, G.J., P. Zhao, and W.D. Zhang. Advancements in micro-structure with multiple stress concentration region for bionic vector hydrophone. in Key Engineering Materials. 2015. Trans Tech Publ.
28. 28. Bio-inspired piezoelectric artificial hair cell sensor fabricated by powder injection molding. Han, Jun Sae, Keun Ha Oh, Won Kyu Moon, Kyungseop Kim, Cheeyoung Joh, Hee Seon Seo, Ravi Bollina, and Seong Jin Park. s.l. : Smart Materials and Structures, 2015, Vols. Volume 24, Number 12. DOI 10.1088/0964-1726/24/12/125025.

DOI: 10.46121/pspc.54.1.8

29. 29. Liu, Y., et al., “Lollipop-shaped” high-sensitivity Microelectromechanical Systems vector hydrophone based on Parylene encapsulation. Journal of Applied Physics, 2015. 118(4): p. 044501.
30. 30. Prabhu, Smitha G., and S. Nagabhushana. "Design and Simulation Of Under Water Acoustic Mems Sensor." In COMSOL Conference, Pune. 2015.
31. 31. Design and simulation of MEMS vector hydrophone with reduced cross section based meander beams. Kumar, Manoj, S. Dutta, Ramjay Pal, K. K. Jain, Sudha Gupta, and R. K. Bhan. s.l. : AIP Conference Proceedings, 2016, Vols. vol. 1724, no. 1. https://doi.org/10.1063/1.4945176.
32. 32. Design and realization of sculpture-shaped ciliary MEMS vector hydrophone. Peng Chen, Guojun Zhang, Xi Yang, SongXiang Ji, XiaoQi Liang, Ting Lv, XiaoYong Zhang, Shan Zhu, ZhenZhen Shang, WenDong Zhang. s.l. : Sensors and Actuators A: Physical, 2021, Vol. 331: p. 112575. https://doi.org/10.1016/j.sna.2021.112575.
33. 33. Lv, Ting, Xiaoqi Liang, Guojun Zhang, Shasha Yang, Peng Chen, Xi Yang, Shan Zhu, Zhenzhen Shang, Boyuan Jing, and Wendong Zhang. "Design and implementation of beaded cilia MEMS vector hydrophone." Measurement 182 (2021): 109751.
34. 34. Design and fabrication of Hollow mushroom-like cilia MEMS vector hydrophone. Geng, Yanan, Weirong Ren, Guojun Zhang, Peng Chen, Shan Zhu, Yifan Zhang, Yan Liu et al. s.l. : IEEE Transactions on Instrumentation and Measurement, 2023, Vol. V 72. https://doi.org/10.1109/TIM.2022.3224998.
35. 35. Xu, W., et al., Development of cup-shaped micro-electromechanical systems-based vector hydrophone. Journal of Applied Physics, 2016. 120(12): p. 124502.
36. 36. Xu, Q., et al., Design and implementation of two-component cilia cylinder MEMS vector hydrophone. Sensors and Actuators A: Physical, 2018. 277: p. 142-149.
37. 37. Singh, R., et al. Design and optimization of MEMS-based four beam vector hydrophone for direction of arrival. in International Workshop on the Physics of Semiconductor and Devices. 2019. Springer.
38. 38. Zhang, L., et al., Design and fabrication of a multipurpose cilia cluster MEMS vector hydrophone. Sensors and Actuators A: Physical, 2019. 296: p. 331-339.
39. 39. Filippi, Paul, Aime Bergassoli, Dominique Habault, and Jean Pierre Lefebvre. Acoustics: Basic Physics, Theory, and Methods. USA : Elsevier, 1998. 0-12-256190-2.
40. 40. Safari, A. and E.K. Akdogan, Piezoelectric and acoustic materials for transducer applications. 2008: Springer Science & Business Media.

DOI: 10.46121/pspc.54.1.8